Title
Heterogeneous Dielectric Implicit Membrane Model for the Calculation of MMPBSA Binding Free Energies

Journal
Journal of Chemical Information and Modeling, 59(6)

ISSN
1549-9596

Authors
Greene, D'Artagnan
Qi, Ruxi
Nguyen, Remy
et al.

Publication Date
2019-06-24

DOI
10.1021/acs.jcim.9b00363

Peer reviewed

HHS Public Access

Author manuscript

J Chem Inf Model. Author manuscript; available in PMC 2020 May 04.

Published in final edited form as:

J Chem Inf Model. 2019 June 24; 59(6): 3041–3056. doi:10.1021/acs.jcim.9b00363.

Heterogeneous Dielectric Implicit Membrane Model for the Calculation of MMPBSA Binding Free Energies

D'Artagnan Greene[†], **Ruxi Qi**[†], **Remy Nguyen**[†], **Tianyin Qiu**[‡], **Ray Luo**[*,†,§,‖,⊥,#]

[†]Department of Molecular Biology and Biochemistry, University of California, Irvine, California 92697, United States

[‡]Department of Chemistry, University of California, Irvine, California 92697, United States

[§]Chemical and Materials Physics Graduate Program, University of California, Irvine, California 92697, United States

[‖]Department of Biomedical Engineering, University of California, Irvine, California 92697, United States

[⊥]Department of Chemical and Biomolecular Engineering, University of California, Irvine, California 92697, United States

[#]Department of Materials Science and Engineering, University of California, Irvine, California 92697, United States

Abstract

Membrane-bound protein receptors are a primary biological drug target, but the computational analysis of membrane proteins has been limited. In order to improve molecular mechanics Poisson–Boltzmann surface area (MMPBSA) binding free energy calculations for membrane protein–ligand systems, we have optimized a new heterogeneous dielectric implicit membrane model, with respect to free energy simulations in explicit membrane and explicit water, and implemented it into the Amber software suite. This new model supersedes our previous uniform, single dielectric implicit membrane model by allowing the dielectric constant to vary with depth within the membrane. We calculated MMPBSA binding free energies for the human purinergic platelet receptor ($P2Y_{12}R$) and two of the muscarinic acetylcholine receptors (M2R and M3R) bound to various antagonist ligands using both membrane models, and we found that the heterogeneous dielectric membrane model has a stronger correlation with experimental binding affinities compared to the older model under otherwise identical conditions. This improved membrane model increases the utility of MMPBSA calculations for the rational design and improvement of future drug candidates.

[*]Corresponding Author: (R.L.) rluo@uci.edu.

Supporting Information

The Supporting Information is available free of charge on the ACS Publications website at DOI: 10.1021/acs.jcim.9b00363. Tables containing BAR convergence data, explicit BAR free energy calculation results, and redocked compound 6B MMPBSA results and figures containing a diagram of our DMPC membrane model, amino acid distributions for membrane proteins within a given *z*-value range, the formation of a membrane defect for charged residues, the equations for our two dielectric membrane fitting profiles, and convergence plots for the MMPBSA values obtained in our $P2Y_{12}R$ and M2R/M3R test systems (PDF)

The authors declare no competing financial interest.

INTRODUCTION

Membrane proteins connect the internal environment of a cell to the surrounding medium. In doing so, they act as receptors of extracellular ligands, transporters that allow the passage of small molecules, enzymes that catalyze chemical reactions, and more.[1] The accessibility of membrane-bound protein receptors on the cell surface has made them a primary biological drug target. It is estimated that nearly 40% of all drug targets are either class I G-protein coupled receptors or nuclear receptors while 60% of all drug targets appear on the cell surface.[2]

In rational drug design efforts, the computational analysis of protein–ligand binding affinities has become an important tool. Efficient, implicit solvent-based methods for modeling globular protein–ligand binding have been employed for many years, but the extension of such methods to membrane protein–ligand binding is far less developed despite its pharmacological importance. A complication that has held back the development of implicit solvent models for membrane proteins is that they are much more difficult to implement; the surrounding membrane must be taken into account along with the aqueous environment in the solvation model. Another factor is that the total number of membrane protein crystal structures available in the RCSB Protein Data Bank (PDB) is less than 3% of the total number of proteins deposited in the database.[3,4] This reflects the experimental difficulties in obtaining viable structures of membrane-bound proteins.[5] Nevertheless, over 92% of current drug targets are reported to be similar to known proteins in the PDB, which suggests a strong structural coverage of druggable membrane proteins for use in rational drug design.[2] In addition, methodological improvements to cryo-electron microscopy (cryo-EM) within the past few years have opened up the possibility that several high-profile membrane proteins which have resisted crystallization will be available for study in the near future.[6]

Recently, our lab implemented an implicit membrane model into the Amber 16 software suite[7,8] that allowed users to calculate the molecular mechanics Poisson–Boltzmann surface area (MMPBSA) binding free energy of a membrane protein–ligand system.[9–12] PBSA-based implicit solvent models have been used in a wide variety of biological applications including the prediction of pK_a shifts,[13,14] solvation free energies,[15–18] protein folding,[19–26] and binding free energies.[27–30] In PBSA calculations, the electrostatic interaction term is calculated using the Poisson–Boltzmann equation (PBE),[31–36] which is frequently approximated as the linear PBE:

$$\nabla \cdot \varepsilon \nabla \phi = -4\pi\rho_0 + \varepsilon_v \kappa^2 \phi \tag{1}$$

where $\kappa^2 = \frac{8\pi e^2 I}{\varepsilon_v k_B T}$. In eq 1, v refers to the solvent, and the ionic strength is given as $I = z^2 c$. It can be seen in eq 1 that the PBE has a dependency on the dielectric constant (ε), and an accurate selection of the dielectric constant will therefore have a direct impact on the accuracy of the overall PBSA calculation.

In Amber 16, our implicit membrane was modeled as a uniform slab with a single, low dielectric constant. While an important first step, a single dielectric implicit membrane

model cannot effectively reconcile the low dielectric membrane core region, which consists of long nonpolar hydrocarbon tails, with the high dielectric membrane periphery region, which contains polar and charged headgroups.[37–39] The hydrophobic core of the membrane has been described as having a low dielectric constant of around 2, while the polar headgroup region of the membrane has been reported as having a much higher dielectric constant, with estimates in the range of 80–1000.[39,40] It has been demonstrated that these different dielectric properties can affect the interactions of small molecules with the membrane at different depths within the membrane. For instance, this difference in membrane structure can lead to qualitatively different permeabilities at different depths within the membrane when compared to membranes consisting of more uniformly structured alkane components.[38,41–45] This is especially a concern for our intended application as many binding interactions take place at the interface between water and protein at the periphery, in the vicinity of phospholipid headgroups, as opposed to in the low dielectric membrane interior.

The inherent inaccuracies of using a single dielectric membrane model can be lessened by implementing a heterogeneous dielectric membrane model that assigns a local dielectric constant that varies with depth within the phospholipid membrane (Figure 1).[46–50] Here, we introduce such a heterogeneous dielectric implicit membrane model into Amber 18. In our present approach, we calibrate our implicit membrane model by calculating the free energy of decharging the side chains of all 20 common amino acid residues at a given depth within the membrane. The optimal dielectric constant at a given depth is obtained from the global minimum of the root-mean-square deviation (RMSD) between the free energy for decharging that is calculated in both the implicit and explicit membrane. This approach follows the philosophy of modern force field development by focusing on model compounds. In this case, we calibrate a variable dielectric profile in our implicit membrane model using a full set of parametrized amino acid side chains to represent the chemical properties of full-size membrane proteins. Of course, subsequent studies should pay attention to the transferability of the new implicit membrane model to different protein and ligand molecules, akin to what has been done for explicit membrane models. This current approach does allow for a more direct calibration of the membrane compared to prior methods which used a generic test charge.[39,40,48]

The implementation of a heterogeneous dielectric implicit membrane model into the Amber PBSA framework is aimed at creating a much more accurate membrane environment for MMPBSA binding free energy calculations of membrane protein–ligand systems. To examine the impact of the new membrane model on this calculation for a few relevant test cases, we have calculated MMPBSA binding free energies for two G-protein coupled receptor systems, the human purinergic platelet receptor ($P2Y_{12}R$) and two muscarinic acetylcholine receptors (M2R and M3R) bound to various antagonist ligands, using both the new heterogeneous dielectric membrane model and the old uniform dielectric membrane model. $P2Y_{12}R$ is a prominent membrane bound receptor that is targeted for platelet aggregation inhibition in the treatment of myocardial infarction and stroke. Several antithrombotic drugs target $P2Y_{12}R$, but limitations of these drugs have motivated the development of a new generation of $P2Y_{12}R$ inhibitors.[51–53] The muscarinic acetylcholine receptor M3R is a target for antagonist drugs involved in treating chronic pulmonary disease.

A desire to enhance selectivity for M3R over the structurally similar M2R subtype, which modulates heart rate, has fueled a structure-guided approach to antagonist ligand design.[54] For our membrane comparison, the $P2Y_{12}R$ receptor has an open binding site that is exposed to water (Figure 2) whereas the closed binding site for M2R and M3R is buried a bit deeper into the membrane (Figure 3). These systems allow us to test the performance of our MMPBSA calculations at different depths within our membrane models. In the future, computational modeling may play a key role in the drug design process, and here we demonstrate how our improved membrane model increases the accuracy of MMPBSA calculations which can be used in the rational design of future drug candidates.

METHODS

Preparation of Amino Acid Side Chains.

Our first step toward obtaining a heterogeneous dielectric profile was to calculate the free energy difference for decharging an amino acid side chain, from 100% of its original charge to 0% of its original charge, at a given depth within an explicit all-atom membrane model. With the exception of glycine and proline, each amino acid in the standard library in Amber was edited using XLEAP to remove the common peptide backbone from the amino acid, isolating each amino acid side chain. For each isolated amino acid side chain, a proton was added to the β-carbon. The charge on the added proton was adjusted to match that of other β-carbon protons, and the charge on the β-carbon itself was adjusted to give the side chain as a whole the correct total net charge of the natural side chain at pH = 7.[55] Glycine and proline were unedited due to the lack of a β-carbon for glycine, and due to the cyclization of the side chain and backbone in the case of proline. These two amino acids were used to test the effect of decharging the peptide backbone.

z-Restraint, Decharging MD Simulations in Explicit Solvent.

Each amino acid side chain was placed into a model membrane to perform *z*-restraint simulations where the center of mass of the side chain was restrained by a square potential at a certain height on the *z*-axis.[38,39,43,56] Our explicit membrane model consisted of 36 1,2-dimyristoyl-*sn*-glycero-3-phospho-choline (DMPC) phospholipids in each leaflet of the bilayer for a total of 72 phospholipids used in the membrane model as a whole (Figure S1). Although the overall length of the DMPC phospholipid is slightly smaller than the more common 1,2-dipalmitoyl-*sn*-glycero-3-phosphocholine (DPPC) phospholipids, DMPC membrane models have been shown to have very similar properties when compared to membrane models that use DPPC phospholipids.[57–59] The explicit DMPC membrane model itself was generated using the CHARMM-GUI membrane builder with the Amber Lipid 14 force field as described in the Amber lipid membrane tutorial.[56,60–62] The membrane was flanked by 1440 TIP3P water molecules on each side of the membrane to fit inside an approximately $50 \times 50 \times 80$ $Å^3$ box.[56] Potassium ions were added to neutralize the system if necessary.

The center of mass of the bilayer membrane was calculated relative to the N31 atom in the phosphatidylcholine headgroup of each phospholipid in the bilayer, and this center of mass was subsequently set as $z = 0$ Å An amino acid side chain was then placed at a certain height

on the *z*-axis relative to the center of mass of the bilayer.[56] We chose to place our side chain at 5 Å intervals along the *z*-axis (at $z = 0$, 5, 10, 15, 20, and 25 Å) to split the membrane into 6 regions for sampling that roughly corresponded to the midpoint of: the hydrocarbon core region (split up into three subregions: 0–2.5, 2.5–7.5, and 7.5–12.5 Å), the hydrocarbon and ester interface region (12.5–17.5 Å), the phosphatidylcholine headgroup region (17.5–22.5 Å), and the bulk water solvent (22.5–27.5 Å) (Figure S1). After a side chain was placed into the membrane model at a given height, a 10 000 step minimization was carried out using 5000 steps of steepest descent followed by 5000 steps of conjugate gradient. The particle mesh Ewald method (PME) was employed with a real space cutoff of 10.0 Å, but otherwise, the default options were used for all solvated simulations. The lipid and amino acid side chain molecules were held fixed as the system was heated in two steps. First, the system was heated from 0 K to approximately 100 K for 5.0 ps using the Langevin thermostat in the *NVT* ensemble. The system was then heated from 100 to 303 K for 100 ps using the Langevin thermostat in the *NPT* ensemble with anisotropic pressure scaling and a pressure relaxation time of 2.0 ps.

After heating, an equilibration step using semi-isotropic pressure scaling was performed whereby all restraints on the lipids were removed while a center of mass restraint was applied to the amino acid side chain at the appropriate *z*-value. This restraint was a harmonic potential (V) of the form:

$$V = k(R - r)^2 \tag{2}$$

where the option was set to apply the restraint only on the *z*-axis, r was set as the target equilibrium *z*-value, the range R of the potential was set to -99 Å $< R <$ +99 Å, and the initial value of the spring constant k was set to 2.5 kcal/(mol Å^2). In order to improve the convergence of our free energy calculations, the spring constant was gradually ramped up during the equilibration step. Specifically, we carried out an initial short equilibration for 20 ps with $k = 2.5$ kcal/(mol Å^2), then an additional short 20 ps equilibration with $k = 25$ kcal/(mol Å^2), and finally, an extensive equilibration was performed for approximately 100 ns with $k = 100$ kcal/(mol Å^2). Subsequent free energy calculations demonstrated that, if the results had converged properly within the time frame of the calculation, ramping up the spring constant in this way did not appreciably alter the calculated free energy values (Table S1).

After equilibration, we proceeded to uniformly reduce the charges on all of the atoms in the amino acid side chain from 100% to 0% in successive 10% decrements. For each 10% reduction in charge, MD simulations in the *NVT* ensemble were carried out in 20 ns intervals. From each 20 ns trajectory, the first 10 ns was discarded, and the second 10 ns was retained for use in our subsequent free energy calculations. For the free energy calculations, a total of 1000 snapshots, taken at equal intervals from each of the retained 10 ns trajectories, were used for analysis where the energy was extracted from each snapshot using SANDER in Amber 18. Here, 20 ns for each interval was deemed sufficient for such calculations; doubling our data collection to 40 ns for each interval and using 20 ns for the free energy calculations did not substantially change our results (Table S2). In addition, our inspection of the saved trajectories revealed that bulky side chains such as tryptophan and

tyrosine were sampling different orientations during the decharging runs, which is an apparent concern for studying these molecules in the membrane environment. We did encounter difficulties obtaining converged free energy values at times, for example some data points for charged residues (Table S2) had clear deviations when comparing our 20 and 40 ns data. Nevertheless, our total simulation times of 300 ns (using 20 ns steps) and 500 ns (using 40 ns steps) were among the longest used for calculations of this type, and even in a few worst-case scenarios, the calculated free energy values converged to within a few kcal/mol.

BAR Free Energy Calculations in Explicit Solvent.

To further assist with the convergence of our free energy calculations, we used the Bennet acceptance ratio (BAR) calculation to calculate the free energy difference for each 10% decharging decrement.[63] The BAR calculation can be described as a self-consistency problem where the value of C is chosen to best satisfy the following relations:

$$\Delta G = \ln \frac{\sum_j f(U_i - U_j + C)}{\sum_i f(U_j - U_i + C)} + C \tag{3}$$

$$\Delta G = C \tag{4}$$

$$f(x) = 1/(1 + e^x) \tag{5}$$

where i refers to the initial state and j to the final state for any two consecutive states in the decharging procedure, and where an equal number of frames was sampled in each state. Here, $U_i - U_j$ in $\Sigma_j f(U_i - U_j + C)$ refers to the difference in energy values calculated for each of the 1000 frames in the ensemble of trajectory j (trajectory j is the MD trajectory of the amino acid side chain at the final, 10% lower, charge) where the energies were calculated using both sets of charges (U_i representing the energy calculated using the higher charge and U_j the energy calculated using the 10% lower charge). Similarly, $U_j - U_i$ in $\Sigma_i f(U_j - U_i + C)$ refers to the difference in energy values calculated for each of the 1000 frames in the ensemble of trajectory i (trajectory i is the MD trajectory of the amino acid side chain at the initial, higher charge) with the energies calculated using the initial (U_i) and final (U_j) charges as described previously. C is then a fitting parameter which is chosen in order to satisfy eqs 3 and 4. The total cost of decharging an amino acid side chain from 100% to 0% can then be obtained by summing over all of the decharging decrements in the entire data set:

$$\Delta G_{\text{total}} = \sum_k \Delta G_k \tag{6}$$

with each ΔG_k representing the change in free energy for a step involving a 10% decrease in the charge of an amino acid side chain.

PBSA-BAR Free Energy Calculations in Implicit Solvent.

Using our uniform, single dielectric implicit membrane model, we calculated the total free energy of decharging an amino acid side chain from 100% to 0% at a given *z*-value using the PBSA-BAR procedure.[64] Our goal was to perform this calculation for a large number of different dielectric constants to find out which dielectric constant was optimal at a given *z*-value. Since the number of individual PBSA calculations that needed to be carried out was large, we reduced the number of frames for each individual calculation from 1000 to about 50 evenly spaced frames from the original trajectory. In the 50 processed trajectory frames, autoimaging was used to center the trajectory frames at the C110 atom located in a myristoyl group near the center of the lipid bilayer, and all ions, water, and explicit membrane molecules were removed.

For the PBSA calculations,[65–78] a 120 × 120 × 160 $Å^3$ box was constructed with the amino acid side chain placed relative to the previously calculated center of mass of the membrane. In addition to using a large box size, we also increased the ratio between the dimension of the finite-difference grid and that of the solute bounding box to 4.0 for this portion of the analysis, following the recommendation in the Amber manual for small ligand systems. The implicit membrane thickness was obtained by calculating the average explicit membrane thickness over the whole trajectory. This was accomplished by calculating the location of the center of mass of the N31 atoms in the phosphatidylcholine headgroups at the top of the membrane, repeating the same calculation for the bottom of the membrane, and taking the difference between the two. The protein and aqueous solvent dielectric constants were set at 1 and 80 respectively while the membrane dielectric constant was changed for each separate run. The aqueous solvent probe was set to 1.4 Å while the membrane solvent probe was set to 2.70 Å.[12]

For each individual amino acid side chain in the bulk water solvent at $z = 25$ Å, the radii of the side chain atoms were uniformly scaled to give the minimum difference in the total free energy for decharging the side chain in explicit and implicit solvents. This optimized radius scaling factor was then used for all subsequent PBSA calculations at all other z-values. Using SANDER, the energy from PBSA calculations was extracted from the trajectory snapshots, and eqs 3–6 were used to calculate ΔG_{total} as described previously.

RMSD Calculations.

As a quantitative estimate of the error at a given *z*-value between the explicit and implicit ΔG_{total} results, we calculated the root-mean-square deviation (RMSD) across our data set of amino acid side chains using the standard formula:

$$\text{RMSD} = \sqrt{\frac{\sum_i \left(\Delta G_{\text{total(implicit)}i} - \Delta G_{\text{total(explicit)}i}\right)^2}{N}} \tag{7}$$

where i represents amino acid i and where N represents the total number of amino acids included in the calculation (taken to be either 20 or 15 depending on whether acidic and basic amino acids were included in the calculation). Equation 7 was used to calculate the RMSD for our free energy calculations at different membrane dielectric constant values. The

specific value of the membrane dielectric constant that gave the minimum RMSD at a given z-value was taken to be the best fit membrane dielectric constant and was used to construct our dielectric profile for the implicit membrane model as a whole.

Implementation of the Dielectric Profile into PBSA.

Given the discrete, z-depth dependent membrane dielectric data set, we performed interpolation using two different schemes to get a smoothed profile. The first scheme was a piecewise cubic Hermite interpolating polynomial (PCHIP) fitting, which passed through all data points.[79] The second scheme was a second-order spline fitting, which generated an overall smoothed fitting but did not necessarily pass through the data points.[80] In addition, to maintain a zero-slope boundary condition in the latter method, we replaced the second-order spline within the fitting range of z = 2.5–5.0 Å with a cubic spline.

The advantage of using a PCHIP fitting over a cubic spline fitting is that the fitted function is smooth enough, but less oscillatory, to capture the monotonic dielectric change inside the membrane. The PCHIP algorithm preserves monotonicity in the interpolation data and does not overshoot if the data is not smooth.[79] However, while the first derivatives are guaranteed to be continuous, the second derivatives may jump at knots. To determine the derivatives f'_k at the points z_k, let $h_k = z_{k+1} - z_k$ and $d_k = (y_{k+1} - y_k)/h_k$ be the slopes at internal points z_k where y_k refers to the dielectric constant. If the signs of d_k and d_{k-1} are different, or either of them equals zero, then $f'_k = 0$. Otherwise, f'_k is given by the weighted harmonic mean:

$$\frac{w_1 + w_2}{f'_k} = \frac{w_1}{d_{k-1}} + \frac{w_2}{d_k} \tag{8}$$

where $w_1 = 2h_k + h_{k-1}$ and $w_2 = h_k + 2h_{k-1}$. The end slopes are generally set using a one-sided scheme where in our case both of the end slopes equal zero.[81]

The spline fitting was implemented to get an overall smoothed fitting in a least-squares manner. The fitted spline ($spl(z)$) uses a representation in the B-spline basis. In our case, six B-spline basis functions were constructed for the fitting range of z = 2.5–20.0 Å. The smoothing condition s = 0.01 was used to choose the number of knots that are determined by satisfying:

$$\sum_i w_i \times (y_i - spl(z_i))^2 \leq s \tag{9}$$

where w_i is the weight for spline fitting, which in our case was equal for each i, and y_i is the dielectric constant from our test set. The final spline, $spl(z)$, was constructed using a linear combination of the six B-spline basis functions. The full data range used to fit PCHIP was z = 0–25.0 Å while for the spline it was z = 2.5–20.0 Å. The fitted piecewise functions were coded into the PBSA program in the Amber 18 package. Note that in practice the membrane thickness can vary depending on the membrane model used in the simulation, and so, to match the overall membrane thickness to the user specified thickness value in the software, we allow the inner membrane core region (originally sampled at a z-depth of 0–2.5 Å) to be

stretchable with a dielectric constant of 1.0. The two fittings were implemented in the programs SciPy 1.1.0 and SymPy 1.2.[82,83]

Natural Abundance of Each Amino Acid in Different Membrane Regions.

While analyzing our results, we also calculated the natural abundance of each amino acid found in membrane proteins within our specific z-value ranges using a library of structures downloaded from MemProtMD.[4,58] The purpose for doing this was to examine the abundance of different types of amino acids in each range in order to see the effect of leaving out acidic and basic amino acids from our dielectric profile in the hydrophobic core region. We used a total of 482 MemProtMD structures, representing the bulk of unique MemProtMD structures that were available at the time of our analysis. Redundant structures that were available on MemProtMD, and a few abnormal structures where the protein had clearly not been placed properly within the membrane, were not included in our analysis.

Each MemProtMD structure was centered at $z = 0$ Å by subtracting the average z-coordinate of all membrane atoms from the original z-coordinate of each individual atom in the structure file. Individual amino acid residues from the membrane proteins were sorted into 5 bins depending on their location along the z-axis (corresponding to bins of 0–2.5, 2.5–7.5, 7.5–12.5, 12.5–17.5, and 17.5–22.5 Å), and we counted the number of amino acid residues that appeared in each bin. The probability that a specific amino acid appeared within a given z-value range was taken as the number of times that it appeared divided by the sum of all 20 amino acids that appeared within that range, i.e.

$$p_i = \frac{m_i}{\sum_i m_i} \tag{10}$$

where p_i represents the probability of finding amino acid i, m_i is the total number of times that amino acid i appeared within the specified z-value range, and the sum is taken over all 20 amino acids.

It should be noted at this point that additional complications to this calculation, such as distinguishing between external amino acids on the surface of the protein and internal amino acids on the protein interior and separating α-helical transmembrane proteins from β-barrel transmembrane proteins, were not explicitly taken into account in our analysis;[84] our results were averaged over both external and internal amino acids and across both of the main membrane protein types. However, despite this more simplistic approach, we note that our final results (Figure S2) still accurately reflect the observed trends in the distribution of membrane protein amino acids that were reported previously in the literature.[58,84]

MMPBSA Calculations for the $P2Y_{12}R$ and M2R/M3R Test Systems.

To test the effect of the heterogeneous dielectric membrane model on MMPBSA calculations,[85–90] we carried out MMPBSA calculations for the human purinergic platelet receptor ($P2Y_{12}R$) and two muscarinic acetylcholine receptors (M2R and M3R) bound to various antagonist ligands using the MMPBSA.py module in Amber 18. Models of $P2Y_{12}R$ bound to the antagonist ligands: AZD-1283 (AZD), PSB-0739 (PSB), and Ticagrelor (TIQ) were derived from a previously published crystal structure (PDB ID: 4NTJ).[53] Both the

model preparation and the molecular dynamics simulation protocol that we employed for this test system were described in detail in our previous publication.[11]

The M2R and M3R protein models with the antagonist ligands 3-quinuclidinylbenzilate (QNB) and tiotropium were derived from previously available crystal structures (PDB IDs: 4DAJ, 5ZHP, and 3UON). For the M2R model (derived from 3UON), the cytoplasmic domain was cleaved in order to place the center of mass of the protein in close proximity to the center of mass of the model membrane system to facilitate the MMPBSA calculation. The compound 6B antagonist that was used to demonstrate M2R/M3R selectivity by Liu et. al was constructructed by modifying the QNB ligand present in the 3UON crystal structure.[54] The ligands were transplanted from one crystal structure to another by performing an alignment of the M2R and M3R crystal structures using UCSF Chimera[91] before making the substitution of one ligand for another. The parametrization of the antagonist ligands, membrane model preparation (for a 64 × 64 DPPC bilayer), and single trajectory MD simulations were performed in the usual way based on the Amber lipid membrane tutorial and other standard MD and MMPBSA protocols as described previously.[11,61] For the $P2Y_{12}R$ system, we used a 20 ns equilibration step which was followed by a 10 ns production step, and 1000 evenly spaced frames from the production step were used in our MMPBSA calculations. Due to the use of a docked complex in our M2R and M3R analysis, we increased the equilibration step to 90 ns before carrying out a 10 ns production step. This was followed by the extraction of 1000 evenly spaced frames from the production step for our MMPBSA analysis.

For the MMPBSA calculations for both systems, we tested three implicit membrane models: the uniform, single dielectric membrane model with the membrane dielectric constant set to 4, the heterogeneous dielectric membrane model using the PCHIP fitting, and the heterogeneous dielectric membrane model using the spline fitting. The average membrane thickness was calculated relative to the N31 atoms in the explicit phospholipid membrane as described above. Other PB settings were as follows: the protein dielectric constant was set to 2, the ionic strength was set to 150 mM, the ratio between the dimension of the finite-difference grid and that of the solute bounding box was set to 1.5, the geometric multigrid solver was used to solve the linear systems,[10] electrostatic focusing was switched off, periodic boundary conditions were used, the atom-based cutoff distance to remove short ranged finite difference interactions and to add pairwise charge-based interactions was set to 7.0 Å, the atom-based cutoff distance for van der Waals interactions was set to 99.0 Å, the total electrostatic energies and forces were computed using the particle–particle particle-mesh (P3M) procedure,[92] Bondi radii from the parameter topology file were used, and the pore searching algorithm was turned off. All other PB parameters were set to their default values in MMPBSA.py for Amber 18. Our binding affinity modeling was carried out without the optional normal mode entropy analysis as this analysis usually does not contribute favorably to the overall agreement with experiment due to the approximation used.[89,93,94] Our results were compared to experimental binding free energies published in the literature.[53,54]

RESULTS AND DISCUSSION

BAR Results for Decharging Amino Acid Side Chains in an Explicit Membrane.

Before turning to our implicit membrane models, we first examine the BAR results obtained from an analysis of our explicit all-atom MD simulations. As calculated using the BAR method, the total free energy change, ΔG_{total}, for decharging a given amino acid side chain from 100% to 0% as a function of the z-value (with $z = 0$ Å corresponding to a plane at the center of the membrane bilayer) is given in Tables S3 and S4. From the data, we see that the ΔG_{total} values were at a minimum at the center of the membrane ($z = 0$ Å) and reached a maximum in the polar headgroup region ($z = 20$ Å) or in the bulk aqueous solvent ($z = 25$ Å) for all amino acids regardless of their type.

Note that the ΔG values given in Tables S3 and S4 include both Coulomb and reaction field contributions. This makes comparisons of reaction field energies between various amino acid side chains difficult. This is not important for our optimization of the membrane model, but focusing on reaction field energies helps us to compare our results to the literature values to assess the accuracy of our approach. To focus on the reaction field energies, we used the data in Tables S3 and S4 to calculate the relative ΔG_{total} values between placing each amino acid side chain at the center of the membrane, which approximates a low dielectric vacuum environment (see Table 1) with a relatively large accessible free volume,[95] and at any other z-value using

$$\Delta\Delta G_{\text{total}(z_i)} = \Delta G_{\text{total}(z_i)} - \Delta G_{\text{total}(z = 0\ \text{Å})} \tag{11}$$

where $\Delta G_{\text{total (z=0 Å)}}$ represents the ΔG_{total} value for a given amino acid side chain at z = 0 Å in Table S3 or S4, and $\Delta G_{\text{total}(z_i)}$ represents the ΔG_{total} value for that side chain at z = i in Table S3 or S4, where i can take on values of z = 0, 5, 10, 15, 20, or 25 Å. $\Delta G_{\text{total}(z_i)}$ is the relevant quantity to use to analyze reaction field energies.

The numerical values obtained by performing this calculation are given in Tables S5 and S6, and a plot of $\Delta\Delta G_{\text{total}}$ vs z for each amino acid is given in Figure 4. From Figure 4, we can see that the increase in $\Delta\Delta G_{\text{total}}$ at higher z-values tends to depend on the net overall charge of the amino acid type, with a smaller dependence on the structural differences between individual amino acid side chains. For example, the top four amino acids in Figure 4 correspond to the four fully charged amino acids. Other amino acids cluster similarly by type. We note that glycine and proline were both used to test the effect of the amino acid backbone as it was not removed for either residue, and the polarity of the backbone likely earned both residues inclusion into a more polar group.

The overall trend in Figure 4 seems clear: the more polar the amino acid side chain, the more expensive the free energy penalty to decharge that side chain in a more polar environment at higher values of z. This result seems reasonable as decharging a charged amino acid side chain in water ($z = 25$ Å) from 100% to 0% effectively means removing favorable interactions between the charged side chain and water while replacing them with less favorable interactions between the decharged, now nonpolar, side chain and water. On the

other hand, decharging an inherently nonpolar amino acid side chain in water does not incur the same penalty as the nonpolar side chain already has nearly zero net charge to begin with. Placing charged side chains deeper into the membrane environment progressively lessens the penalty for decharging the side chain in all cases. In this case, the fully decharged side chain ends up in a more favorable, similarly nonpolar membrane environment regardless of its initial charge characteristics.

Our results are in good agreement with amino acid insertion free energy profiles reported in the literature. Bemporad in 2004[43] reported a maximum difference in free energy of insertion of 0–10 kcal/mol for nonpolar molecules and 15–25 kcal/mol for polar molecules using the CHARMM force field. Tieleman in 2009[55] reported a maximum difference of approximately 2–5 kcal/mol for nonpolar residues, 3–7 kcal/mol for polar and aromatic residues, and 12–20 kcal/mol for charged residues. A more recent, 2017 comparison[96] of free energy insertion profiles using modern versions of the GROMOS, CHARMM, and Amber force fields gave maximum free energy difference estimates of 0–10 kcal/mol for nonpolar, aromatic, and polar amino acids and 10–15 kcal/mol for charged amino acids using Amber 14. All of these results are consistent with our maximum $\Delta\Delta G_{\text{total}}$ results at z = 25 Å (see Figure 4 and Tables S5 and S6).

The accuracy of current free energy calculation methods is subject to improvement. For the calibration of our new heterogeneous dielectric membrane model, we employ standard free energy calculation techniques that facilitate comparisons with our past work, but we note that improvements that address issues with these calculations, such as electrostatic artifacts that arise with the use of periodic boundary conditions (PBC) with the PME method are actively being addressed in recent years.[97–99] Here we have tried to minimize the impact of such artifacts by using large box sizes and increasing the size of the fill ratio used in our PBSA calculations. In addition, note that our free energy difference calculations only consider the effect of decharging the solute; the total free energy change should also take into account cavity formation and the van der Waals interactions. The calibration of these nonpolar terms is a subject that will be addressed in a future study.

PBSA Results for Decharging Amino Acid Side Chains in an Implicit Membrane.

After obtaining our MD trajectories from decharging each amino acid side chain from 100% to 0% at a given z-value, we also calculated ΔG_{total} at that z-value for each amino acid side chain using different values of the membrane dielectric constant while employing our uniform, single dielectric implicit membrane model and the PBSA module. Following this, eq 7 was used to calculate the RMSD between the implicit PBSA-BAR results and the explicit BAR results at each z-value for each dielectric constant that we used. The results for the RMSD calculation are plotted in Figure 5. From Figure 5, the value of the dielectric constant that led to a minimum in the RMSD plot at a given z-value was taken as the optimum dielectric to use at that z-value. The optimized dielectric values obtained from these plots at the given z-values (Figure 5A–E) are listed in Table 1.

Note that a disparity existed between the optimized dielectric values for the full set of 20 amino acids in the first method (method 1) versus the values obtained when acidic and basic amino acids were excluded from the calculation (method 2). Dielectric values in method 1

were generally higher than those in method 2 inside the membrane until the trend reversed in the headgroup region of the membrane. The higher value of the dielectric constants in the membrane interior when charged amino acids were included (method 1) was likely caused by a larger penetration of water, owing to the well-studied formation of water defects when charged groups are restrained within the membrane (Figure S3).[57,100–102] A fair amount of water naturally penetrates into the headgroup region of the membrane to solvate the polar and charged portions of the phospholipid that appear there. Here we see that the optimum dielectric in method 1 for the full set of amino acids converges to a dielectric constant of 80, to match the bulk water solvent as had been assumed in other models of the headgroup region in the past.[48]

The optimum dielectric constant for nonpolar amino acids was consistently lower within the membrane until it suddenly rose sharply to a value that exceeded 200 in the headgroup region. Such a sharp increase in the optimum dielectric constant to 200 or above in the headgroup region had been previously reported in the literature,[39,40] notably as high as 300–1000 when a Lennard-Jones test particle with a small net charge was used as a probe molecule.[39] In our data set, amino acids such as alanine and isoleucine, with very small ΔG_{total} values, did not reach a minimum below a dielectric constant of 200 in the headgroup region. However, the choice of a dielectric constant in this region appears to be less critical than in the hydrophobic core region as raising the dielectric constant from 100 to 200 and above had a minimal effect on the accuracy of our calculated RMSD (Figure 5E). This reflects a slower change in the electrostatic energy at higher dielectric values due to the $1/\varepsilon$ dependence on the calculated energy as pointed out previously by Tanizaki and Feig.[48] Therefore, keeping the dielectric constant at 80 in the headgroup region still seems suitable, as doing so gives a greater benefit to lowering the RMSD when charged amino acids are included than the penalty incurred for using a less-than-optimal dielectric constant for the nonpolar side chains in this region.

To assist us in determining which of the optimal dielectric constants to use for the remaining regions, we calculated the natural abundance of amino acids in each of our sampling regions of the membrane using the majority of the membrane protein structures available in the MemProtMD database. Figure S2 shows that the natural abundance of acidic and basic amino acids in the hydrophobic core region (z = 0–12.5 Å) was low, while it rose noticeably in the polar ester and headgroup regions (z = 12.5–22.5 Å). After considering the large error in the RMSD when charged acidic and basic amino acids were included (see Table 2), we chose to exclude charged amino acids in the hydrophobic core region at z = 0, 5, and 10 Å when determining the optimum dielectric constant. In the polar headgroup region, acidic and basic amino acids were much more abundant, and so we included them in our determination of the optimal dielectric constant at z = 15 and 20 Å. The final dielectric profile that we used is listed in Table 1 as method 3.

Implementation of the Heterogeneous Dielectric Membrane into Amber.

Given the discrete z-depth dependent membrane dielectric data set [(0, 1.0), (2.5, 1.0), (5.0, 0.5), (10.0, 0.25), (15.0, 0.05), (20.0, 0.0125), (25.0, 0.0125)], where (z-value, 1/dielectric) forms a coordinate pair with z = 0 Å defined as the membrane center, we performed an

interpolation using two different schemes to get a smoothed dielectric profile to implement into Amber 18. The fitted curves are shown in Figure 6 while the equations for the fitted profiles are provided in Figure S4. As can be seen in Figure 6, the PCHIP approach intends to be true to the actual data, but leads to a busy profile. The spline approach intends to address the uncertainty in the sampled dielectric constants, which is due to the sampling uncertainty in the free energy simulations, and has a smoother profile.

After the fitted piecewise functions were coded into the PBSA program in Amber 18, we repeated our PBSA-BAR calculations for our set of amino acid side chains using the heterogeneous dielectric membrane with the PCHIP fitting or the spline fitting as our membrane model in place of the uniform dielectric membrane model. The results are presented in Table 2. In Table 2, we see that the global RMSD values calculated using 15 out of 20 amino acids (excluding acidic and basic amino acids) were less than 1 kcal/mol at all z-values within the membrane. When acidic and basic amino acids were included in the calculation, the RMSD values were less than 1 kcal/mol from $z = 15–25$ Å, while it was approximately 1 kcal/mol at $z = 10$ Å Below 10 Å, the RMSD rose sharply in the membrane core when acidic and basic amino acids were included in the calculation. Therefore, as mentioned previously, we chose to exclude charged amino acids from the determination of the optimum dielectric constant in the membrane core region. On the basis of the natural distribution of such amino acids in the hydrophobic core region (Figure S2), we expect this rise in the RMSD in the core region for charged amino acids to not be a major issue for the majority of membrane proteins. Nevertheless, this limitation must be kept in mind as our model would not be expected to perform well if the system of interest explicitly involves buried, charged groups in the hydrophobic core. For such cases, more advanced methods that account for membrane deformation and water penetration into the membrane core need to be implemented.[103–105] In the meantime, the effect of increased water penetration into the membrane for buried charged residues can be crudely approximated using our current model by reducing the value of the membrane thickness in the MMPBSA calculation below that of the true average thickness of the membrane. This would shift the high dielectric region of our implicit membrane model further down into the core of the membrane to account for the deeper penetration of water into the membrane for systems that contain buried charged residues.

MMPBSA Results for the $P2Y_{12}R$ and M2R/M3R Test Systems.

To assess the performance of our new heterogeneous membrane model in comparison to our old uniform membrane model, we carried out MD simulations followed by MMPBSA calculations to calculate the binding free energies for two relevant drug design test systems. The numerical results of our MMPBSA calculations are provided in Tables 3 and 4, correlation plots that compare our results with experimental binding affinities are provided in Figures 7 and 8, and convergence plots for our MMPBSA calculations are available in the Supporting Information (Figures S5–S11). For the human purinergic platelet receptor ($P2Y_{12}R$) bound to various antagonist ligands, Table 3 and Figure 7 reveal that the heterogeneous dielectric membrane models, memopt = 2 and memopt = 3, produced a tighter grouping of data points and a higher correlation with experiment, with $R = 0.92$ and $R = 0.91$ respectively, when compared to the uniform, single dielectric membrane model,

memopt = 1, which had a correlation of $R = 0.59$. We note that the deviation of the slopes from unity and the large values of the *y*-intercepts represent the large systematic errors inherent in MMPBSA free energy calculations when they are compared to experimental binding affinity data. We believe they should be significantly reduced after entropy can be accurately estimated.[90,93] The lack of electronic polarization can also be similarly addressed with residue-specific variable dielectric protein models,[106] and both protein models can be combined together when using the heterogeneous dielectric membrane model in the future.

For the M2R and M3R receptors bound to a variety of antagonist ligands, Table 4 and Figure 8 reveal similar trends in that five out of the six data points using the new model cluster closer together leading to a higher correlation with experiment of $R = 0.72$ and $R = 0.73$, using memopt = 2 and 3 respectively, when compared to the uniform, single dielectric membrane model, memopt = 1, which had a correlation of $R = 0.49$. One data point for the M2R receptor bound to compound 6B was excluded from Figure 8 as its calculated MMPBSA binding free energy was a far outlier in comparison to the rest of the trend (see Table 4). Our MMPBSA calculation predicted that compound 6B should bind slightly stronger to M2R than M3R whereas the experimental result has compound 6B binding to M3R with a K_i of 0.2 nM and to M2R with a much weaker binding affinity, indicated by a K_i of 21 nM. However, we note that experimentally the drug compound 1B (which was a designed precursor to compound 6B) had a binding affinity for M2R that was greater than it was for M3R with K_i values of 0.19 nM and 0.63 nM respectively, closer to what we observed in our MMPBSA calculations.[54]

Li et al. interpreted the difference in the foregoing experimental binding affinity results for compound 1B and compound 6B as having to do with the flexibility of an aromatic ring in compound 1B that could adopt a conformation that interacted via π-stacking with a phenylalanine in the active site of M2R. Compound 6B was designed to be conformationally restricted in order to prevent this interaction in M2R, and this was a factor that led to a large decrease in binding affinity for M2R when comparing the two compounds.[54] The focus on a specific phenylalanine residue was based on the observation that the active site of M3R is structurally almost identical to M2R except for the replacement of this phenylalanine residue with a leucine residue in M3R.

We did not see such an effect lowering the binding affinity of compound 6B for M2R in comparison to M3R in our MMPBSA binding free energy calculations. One reason may have to do with one of the underlying assumptions when using the single trajectory MD method for our MMPBSA calculations, which is that the sampled states of the bound conformations of both the protein and ligand in the complex are assumed to be similar to the conformations of the apoprotein and ligand in solution.[107,108] It seems reasonable to suggest that this assumption would probably not hold up well in a case where the ligand suffers from a conformational restriction that apparently only manifests itself in the M2R but not in the structurally very similar M3R active site.

Perhaps another limitation of our study is that we started our MD simulations using the prefitted active site conformations for both the protein and ligand geometries that were observed in the original crystal structures. We did not have the true binding pose of

compound 6B available from our crystal structures, and so we constructed it using the known binding pose of QNB from the crystal structure 3UON. This is a reasonable starting point if the crystal structure represents the “true” binding pose of the ligand in the active site, but it also introduces a bias in that the system will have a tendency to fluctuate about the conformation present in the original crystal structure while perhaps being kinetically excluded from sampling different conformations that might be relevant in the true binding interaction.

In an attempt to test the effect of introducing a potential conformational bias into our analysis, we erased the “QNB memory” of the active site binding pose for compound 6B by minimizing the conformation of compound 6B in a protein-free, vacuum environment. We then redocked compound 6B into the active site of M2R and M3R using Autodock Vina/SMINA.[109] In Figure 9, the initial binding pose is seen to be qualitatively similar using either method when viewed after minimization and prior to the start of our MD simulations. However, by the end of our production run, it can be seen that noticeable differences in the final binding pose are apparent when comparing the two methods. In Figure 9, noticeable changes in the receptor structures are also apparent as the loops above the active site are shifted depending on which method was used to place compound 6B into the active site at the start of the simulation.

The MMPBSA results after redocking compound 6B, given in Table S7, also revealed a noticeable difference in binding affinity compared to our earlier approach, but the results overall were still somewhat inconclusive. On one hand, the MMPBSA binding free energy for the redocked compound 6B bound to M2R increased by about 39% for memopt = 1 and 21% for memopt = 2 and 3 over the values given when using QNB as a reference for the initial pose, clearly showing that using even a slightly different initial binding pose at the start of the MD simulation can have an effect on our final calculated result. In addition, the increase in binding free energy for compound 6B bound to M2R brought the calculated MMPBSA value into much closer agreement with the rest of the trend established in Figure 8. However, the MMPBSA binding free energy for the redocked compound 6B bound to M3R also increased similarly, by 33% for memopt = 1 and 19% for memopt = 2 and 3. We note that this change was slightly more pronounced for M2R than it was for M3R. This difference restored the proper order of binding between the two ligands when using the new membrane model as compound 6B was now shown to be binding at a higher affinity to M3R in comparison to M2R as expected from the experimental results (Table S7). However, the numerical values of the two MMPBSA calculations were still within 1 kcal/mol of each other after redocking using the new membrane model. Even though their relative binding order had switched, these close numerical values still predict that the binding affinity of compound 6B to M2R and M3R should be similar based on the rest of our trend in Figure 8. This does not agree with the much larger gap in affinity that was observed experimentally. Our results do suggest that the binding affinity is very sensitive to the positioning of compound 6B in the active site and that subtle differences in the ability of M2R and M3R to accommodate the shape of compound 6B may lead to noticeable structural differences in the positioning of loop regions near the active site of the receptor.

For the present purpose of comparing the performance of our heterogeneous dielectric and uniform dielectric membrane models using the standard single trajectory MD and MMPBSA approach, this one data point was a far outlier using either membrane model. Omitting it from our analysis should not grossly alter the present trends that we have observed in the comparison of our two membrane models in both Figure 7 and Figure 8, which contained 11 other data points spread across our three model systems. In the future, more extensive studies will have to be carried out to assess the performance of these two membrane models on a wider variety of systems.

CONCLUSION

The use of MMPBSA binding free energy calculations for membrane protein–ligand systems in rational drug design is likely to increase in the near future. This is due to the pharmacological importance of membrane-bound protein receptors as drug targets and to improved methodology in cryo-EM that will rapidly contribute to the repository of membrane protein structures available for computational studies. In anticipation of an increasing demand for MMPBSA calculations for membrane proteins, we have implemented a heterogeneous dielectric implicit membrane model into the Amber software suite. We obtained our depth-dependent dielectric profile for this new model by minimizing the RMSD between the results of explicit and implicit free energy calculations at various depths within the membrane model. This model supersedes our previous uniform, single dielectric implicit membrane model with a more physical definition of a depth-dependent dielectric profile, and we showed that our new heterogeneous dielectric membrane model can lead to an improved correlation for a series of antagonist ligands bound to the $P2Y_{12}R$ and M2R/M3R test systems when compared to the correlation obtained using the old uniform dielectric membrane model under otherwise identical conditions.

Our heterogeneous membrane model has addressed a few major shortcomings in our prior approach using the single dielectric membrane model.[11] Although we had obtained a good agreement with experimental binding affinities for our $P2Y_{12}R$ test system in our prior study, our simple membrane model was unphysical in that our ligands had to be placed outside of the membrane environment to simulate the lack of a polar headgroup region in our single dielectric membrane model. If the user was to use the actual average thickness of the membrane as a parameter in the MMPBSA calculations, we observed that the agreement with experimental binding affinities decreased, since in reality our ligands actually did bind within the membrane in the polar headgroup and ester regions. In our old model, inserting our ligand within the membrane region placed it into a low dielectric environment of 1–4 instead of in an environment of 20–80 to match the true dielectric environment of the ligand when bound in the active site.

In addition to creating a more realistic and physical depth-dependent model, this new model also avoids complications with the old model that can greatly influence the accuracy of MMPBSA free energy calculations, such as fluctuations in the *z*-axis positions of atoms that may appear within the sampling trajectory of the bound ligand. In the old model, the dielectric constant would change sharply from a high dielectric constant of 80 to a low

dielectric constant of 1–4 at the interface between membrane and water, whereas in the new heterogeneous model, this transition gradually takes place over a distance of about 10 Å.

The potential for developing an automated process for carrying out MMPBSA calculations using the new membrane model will likely prove to be important for rational drug design efforts. To increase the utility of the method, the user needs to be able to place a ligand in an accurate environment for MMPBSA calculations without having to do a lot of manual adjusting of the local dielectric environment while still obtaining physical, meaningful results. Our current model is a step in that direction, and this model can be further improved by calibrating the nonpolar contribution to the free energy calculations in a depth-dependent manner and treating other aspects such as entropy and polarization in the future.

Supplementary Material

Refer to Web version on PubMed Central for supplementary material.

ACKNOWLEDGMENTS

This work was supported by the National Institute of Health/NIGMS (GM093040 and GM079383).

REFERENCES

(1). Almen MS; Nordstrom KJ; Fredriksson R; Schioth HB Mapping the Human Membrane Proteome: A Majority of the Human Membrane Proteins can be Classified According to Function and Evolutionary Origin. BMC Biol 2009, 7, 50. [PubMed: 19678920]

(2). Overington JP; Al-Lazikani B; Hopkins AL How Many Drug Targets are There? Nat. Rev. Drug Discovery 2006, 5, 993–996. [PubMed: 17139284]

(3). Berman HM; Westbrook J; Feng Z; Gilliland G; Bhat TN; Weissig H; Shindyalov IN; Bourne PE The Protein Data Bank. Nucleic Acids Res 2000, 28, 235–242. [PubMed: 10592235]

(4). White S Membrane Proteins of Known 3D Structure http://blanco.biomol.uci.edu/mpstruc/ (accessed Nov 26, 2018).

(5). Seddon AM; Curnow P; Booth PJ Membrane Proteins, Lipids and Detergents: Not Just a Soap Opera. Biochim. Biophys. Acta, Biomembr 2004, 1666, 105–117.

(6). Rawson S; Davies S; Lippiat JD; Muench SP The Changing Landscape of Membrane Protein Structural Biology Through Developments in Electron Microscopy. Mol. Membr. Biol 2016, 33, 12–22. [PubMed: 27608730]

(7). Case DA; Cheatham TE 3rd; Darden T; Gohlke H; Luo R; Merz KM Jr.; Onufriev A; Simmerling C; Wang B; Woods RJ The Amber Biomolecular Simulation Programs. J. Comput. Chem 2005, 26, 1668–1688. [PubMed: 16200636]

(8). Case DA; Ben-Shalom IY; Brozell SR; Cerutti DS; Cheatham TE 3rd; Cruzeiro VWD; Darden TA; Duke RE; Ghoreishi D; Gilson MK; Gohlke H; Goetz AW; Greene D; Harris R; Homeyer N; Izadi S; Kovalenko A; Kurtzman T; Lee TS; LeGrand S; Li P; Lin C; Liu J; Luchko T; Luo R; Mermelstein DJ; Merz KM; Miao Y; Monard G; Nguyen C; Nguyen H; Omelyan I; Onufriev A; Pan F; Qi R; Roe DR; Roitberg A; Sagui C; Schott-Verdugo S; Shen J; Simmerling CL; Smith J; Salomon-Ferrer R; Swails J; Walker RC; Wang J; Wei H; Wolf RM; Wu X; Xiao L; York DM; Kollman PA AMBER 18; University of California, San Francisco, CA, 2018.

(9). Botello-Smith WM; Liu X; Cai Q; Li Z; Zhao H; Luo R Numerical Poisson-Boltzmann Model for Continuum Membrane Systems. Chem. Phys. Lett 2013, 555, 274–281. [PubMed: 23439886]

(10). Botello-Smith WM; Luo R Applications of MMPBSA to Membrane Proteins I: Efficient Numerical Solutions of Periodic Poisson-Boltzmann Equation. J. Chem. inf Model 2015, 55, 2187–2199. [PubMed: 26389966]

(11). Greene D; Botello-Smith WM; Follmer A; Xiao L; Lambros E; Luo R Modeling Membrane Protein-Ligand Binding Interactions: The Human Purinergic Platelet Receptor. J. Phys. Chem. B 2016, 120, 12293–12304. [PubMed: 27934233]

(12). Xiao L; Diao J; Greene D; Wang J; Luo R A Continuum Poisson–Boltzmann Model for Membrane Channel Proteins. J. Chem. Theory Comput 2017, 13, 3398–3412. [PubMed: 28564540]

(13). Georgescu RE; Alexov EG; Gunner MR Combining Conformational Flexibility and Continuum Electrostatics for Calculating pK(a)s in Proteins. Biophys. J 2002, 83, 1731 – 1748. [PubMed: 12324397]

(14). Luo R; Head MS; Moult J; Gilson MK pK(a) Shifts in Small Molecules and HIV Protease: Electrostatics and Conformation. J. Am. Chem. Soc 1998, 120, 6138–6146.

(15). Shivakumar D; Deng Y; Roux B Computations of Absolute Solvation Free Energies of Small Molecules Using Explicit and Implicit Solvent Model. J. Chem. Theory Comput 2009, 5, 919–930. [PubMed: 26609601]

(16). Nicholls A; Mobley DL; Guthrie JP; Chodera JD; Bayly CI; Cooper MD; Pande VS Predicting Small-Molecule Solvation Free Energies: An Informal Blind Test for Computational Chemistry. J. Med. Chem 2008, 51, 769–779. [PubMed: 18215013]

(17). Tan C; Yang L; Luo R How Well Does Poisson-Boltzmann Implicit Solvent Agree with Explicit Solvent? A Quantitative Analysis. J. Phys. Chem. B 2006, 110, 18680–18687. [PubMed: 16970499]

(18). Tan C; Tan YH; Luo R Implicit Nonpolar Solvent Models. J. Phys. Chem. B 2007, 111, 12263–12274. [PubMed: 17918880]

(19). Wen EZ; Luo R Interplay of Secondary Structures and Side-Chain Contacts in the Denatured State of BBA1. J. Chem. Phys 2004, 121, 2412–2421. [PubMed: 15260796]

(20). Wen EZ; Hsieh MJ; Kollman PA; Luo R Enhanced Ab Initio Protein Folding Simulations in Poisson-Boltzmann Molecular Dynamics with Self-Guiding Forces. J. Mol. Graphics Modell 2004, 22, 415–424.

(21). Lwin TZ; Zhou R; Luo R Is Poisson-Boltzmann Theory Insufficient for Protein Folding Simulations? J. Chem. Phys 2006, 124, 034902. [PubMed: 16438609]

(22). Lwin TZ; Luo R Force Field Influences in Beta-Hairpin Folding Simulations. Protein Sci 2006, 15, 2642–2655. [PubMed: 17075138]

(23). Lwin TZ; Luo R Overcoming Entropic Barrier with Coupled Sampling at Dual Resolutions. J. Chem. Phys 2005, 123, 194904. [PubMed: 16321110]

(24). Tan YH; Chen YM; Ye X; Lu Q; Tretyachenko-Ladokhina V; Yang W; Senear DF; Luo R Molecular Mechanisms of Functional Rescue Mediated by P53 Tumor Suppressor Mutations. Biophys. Chem 2009, 145, 37–44. [PubMed: 19748724]

(25). Wang J; Tan C; Tan YH; Lu Q; Luo R Poisson-Boltzmann Solvents in Molecular Dynamics Simulations. Commun. Comput. Phys 2008, 3, 1010–1031.

(26). Lu Q; Tan YH; Luo R Molecular Dynamics Simulations of p53 DNA-Binding Domain. J. Phys. Chem. B 2007, 111, 11538–11545. [PubMed: 17824689]

(27). Swanson JM; Henchman RH; McCammon JA Revisiting Free Energy Calculations: A Theoretical Connection to MM/PBSA and Direct Calculation of the Association Free Energy. Biophys. J 2004, 86, 67–74. [PubMed: 14695250]

(28). Bertonati C; Honig B; Alexov E Poisson-Boltzmann Calculations of Nonspecific Salt Effects on Protein-Protein Binding Free Energies. Biophys. J 2007, 92, 1891 – 1899. [PubMed: 17208980]

(29). Luo R; Gilson MK Synthetic Adenine Receptors: Direct Calculation of Binding Affinity and Entropy. J. Am. Chem. Soc 2000, 122, 2934–2937.

(30). Luo R; Head MS; Given JA; Gilson MK Nucleic Acid Base-Pairing and N-Methylacetamide Self-Association in Chloroform: Affinity and Conformation. Biophys. Chem 1999, 78, 183–193. [PubMed: 10343387]

(31). Warwicker J; Watson HC Calculation of the Electric Potential in the Active Site Cleft Due to Alpha-Helix Dipoles. J. Mol. Biol 1982, 157, 671–679. [PubMed: 6288964]

(32). Jeancharles A; Nicholls A; Sharp K; Honig B; Tempczyk A; Hendrickson TF; Still WC Electrostatic Contributions to Solvation Energies - Comparison of Free-Energy Perturbation and Continuum Calculations. J. Am. Chem. Soc 1991, 113, 1454–1455.

(33). Edinger SR; Cortis C; Shenkin PS; Friesner RA Solvation Free Energies of Peptides: Comparison of Approximate Continuum Solvation Models with Accurate Solution of the Poisson-Boltzmann Equation. J. Phys. Chem. B 1997, 101, 1190–1197.

(34). Luo R; Moult J; Gilson MK Dielectric Screening Treatment of Electrostatic Solvation. J. Phys. Chem. B 1997, 101, 11226–11236.

(35). Cai Q; Wang J; Zhao HK; Luo R On Removal of Charge Singularity in Poisson-Boltzmann Equation. J. Chem. Phys 2009, 130, 145101. [PubMed: 19368474]

(36). Wang J; Tan CH; Chanco E; Luo R Quantitative Analysis of Poisson-Boltzmann Implicit Solvent in Molecular Dynamics. Phys. Chem. Chem. Phys 2010, 12, 1194–1202. [PubMed: 20094685]

(37). Egberts E; Marrink SJ; Berendsen HJC Molecular Dynamics Simulation of a Phospholipid Membrane. Eur. Biophys. J 1994, 22, 423–436. [PubMed: 8149924]

(38). Marrink SJ; Berendsen HJC Simulation of Water Transport through a Lipid-Membrane. J. Phys. Chem 1994, 98, 4155–4168.

(39). Nymeyer H; Zhou HX A Method to Determine Dielectric Constants in Nonhomogeneous Systems: Application to Biological Membranes. Biophys. J 2008, 94, 1185–1193. [PubMed: 17951302]

(40). Stern HA; Feller SE Calculation of the Dielectric Permittivity Profile for a Nonuniform System: Application to a Lipid Bilayer Simulation. J. Chem. Phys 2003, 118, 3401–3412.

(41). Pohorille A; Wilson MA Excess Chemical Potential of Small Solutes Across Water-Membrane and Water-Hexane Interfaces. J. Chem. Phys 1996, 104, 3760–3773. [PubMed: 11539401]

(42). Marrink SJ; Berendsen HJC Permeation Process of Small Molecules Across Lipid Membranes Studied by Molecular Dynamics Simulations. J. Phys. Chem 1996, 100, 16729–16738.

(43). Bemporad D; Essex JW; Luttmann C Permeation of Small Molecules Through a Lipid Bilayer: A Computer Simulation Study. J. Phys. Chem. B 2004, 108, 4875–4884.

(44). Bemporad D; Luttmann C; Essex JW Computer Simulation of Small Molecule Permeation Across a Lipid Bilayer: Dependence on Bilayer Properties and Solute Volume, Size, and Cross-Sectional Area. Biophys. J 2004, 87, 1 – 13. [PubMed: 15240439]

(45). Pratt LR; Pohorille A Hydrophobic Effects and Modeling of Biophysical Aqueous Solution Interfaces. Chem. Rev 2002, 102, 2671–2692. [PubMed: 12175264]

(46). Im W; Feig M; Brooks CL 3rd. An Implicit Membrane Generalized Born Theory for the Study of Structure, Stability, and Interactions of Membrane Proteins. Biophys. J 2003, 85, 2900–2918. [PubMed: 14581194]

(47). Feig M; Im W; Brooks CL 3rd Implicit Solvation Based on Generalized Born Theory in Different Dielectric Environments. J. Chem. Phys 2004, 120, 903–911. [PubMed: 15267926]

(48). Tanizaki S; Feig M A Generalized Born Formalism for Heterogeneous Dielectric Environments: Application to the Implicit Modeling of Biological Membranes. J. Chem. Phys 2005, 122, 124706. [PubMed: 15836408]

(49). Tanizaki S; Feig M Molecular Dynamics Simulations of Large Integral Membrane Proteins with an Implicit Membrane Model. J. Phys. Chem. B 2006, 110, 548–556. [PubMed: 16471567]

(50). Dutagaci B; Sayadi M; Feig M Heterogeneous Dielectric Generalized Born Model with a Van der Waals Term Provides Improved Association Energetics of Membrane-Embedded Transmembrane Helices. J. Comput. Chem 2017, 38, 1308–1320. [PubMed: 28160300]

(51). Savi P; Zachayus JL; Delesque-Touchard N; Labouret C; Herve C; Uzabiaga MF; Pereillo JM; Culouscou JM; Bono F; Ferrara P; Herbert JM The Active Metabolite of Clopidogrel Disrupts P2Y12 Receptor Oligomers and Partitions Them out of Lipid Rafts. Proc. Natl. Acad. Sci. U. S. A 2006, 103, 11069–11074. [PubMed: 16835302]

(52). Algaier I; Jakubowski JA; Asai F; von Kugelgen I Interaction of the Active Metabolite of Prasugrel, R-138727, with Cysteine 97 and Cysteine 175 of the Human P2Y12 Receptor. J. Thromb. Haemostasis 2008, 6, 1908–1194. [PubMed: 18752581]

(53). Zhang K; Zhang J; Gao ZG; Zhang D; Zhu L; Han GW; Moss SM; Paoletta S; Kiselev E; Lu W; Fenalti G; Zhang W; Müller CE; Yang H; Jiang H; Cherezov V; Katritch V; Jacobson KA;

Stevens RC; Wu B; Zhao Q Structure of the Human P2Y12 Receptor in Complex with an Antithrombotic Drug. Nature 2014, 509, 115–118. [PubMed: 24670650]

(54). Liu H; Hofmann J; Fish I; Schaake B; Eitel K; Bartuschat A; Kaindl J; Rampp H; Banerjee A; Hubner H; Clark MJ; Vincent SG; Fisher JT; Heinrich MR; Hirata K; Liu X; Sunahara RK; Shoichet BK; Kobilka BK; Gmeiner P Structure-Guided Development of Selective M3Muscarinic Acetylcholine Receptor Antagonists. Proc. Natl. Acad. Sci. U. S. A 2018, 115, 12046–12050. [PubMed: 30404914]

(55). MacCallum JL; Bennett WF; Tieleman DP Distribution of Amino Acids in a Lipid Bilayer from Computer Simulations. Biophys. J 2008, 94, 3393–3404. [PubMed: 18212019]

(56). Dickson CJ Amber-Umbrella COM restraint tutorial https://github.com/callumjd/AMBER-Umbrella_COM_restraint_tutorial (accessed Nov 26, 2018).

(57). Li LB; Vorobyov I; Allen TW The Role of Membrane Thickness in Charged Protein-Lipid Interactions. Biochim. Biophys. Acta, Biomembr 2012, 1818, 135–145.

(58). Stansfeld PJ; Goose JE; Caffrey M; Carpenter EP; Parker JL; Newstead S; Sansom MS MemProtMD: Automated Insertion of Membrane Protein Structures into Explicit Lipid Membranes. Structure 2015, 23, 1350–1361. [PubMed: 26073602]

(59). Hogberg CJ; Nikitin AM; Lyubartsev AP Modification of the CHARMM Force Field for DMPC Lipid Bilayer. J. Comput. Chem 2008, 29, 2359–2369. [PubMed: 18512235]

(60). Dickson CJ; Madej BD; Skjevik AA; Betz RM; Teigen K; Gould IR; Walker RC Lipid14: The Amber Lipid Force Field. J. Chem. Theory Comput 2014, 10, 865–879. [PubMed: 24803855]

(61). Madej B; Walker R An Amber Lipid Force Field Tutorial: Lipid, 14th ed.; http://ambermd.org/tutorials/advanced/tutorial16/ (accessed Nov 26, 2018).

(62). Wu EL; Cheng X; Jo S; Rui H; Song KC; Davila-Contreras EM; Qi Y; Lee J; Monje-Galvan V; Venable R; Klauda JB; Im W CHARMM-GUI Membrane Builder Toward Realistic Biological Membrane Simulations. J. Comput. Chem 2014, 35, 1997–2004. [PubMed: 25130509]

(63). Bennett CH Efficient Estimation of Free-Energy Differences from Monte-Carlo Data. J. Comput. Phys 1976, 22, 245–268.

(64). Wang C; Ren P; Luo R Ionic Solution: What Goes Right and Wrong with Continuum Solvation Modeling. J. Phys. Chem. B 2017, 121, 11169–11179. [PubMed: 29164898]

(65). Luo R; David L; Gilson MK Accelerated Poisson-Boltzmann Calculations for Static and Dynamic Systems. J. Comput. Chem 2002, 23, 1244–1253. [PubMed: 12210150]

(66). Lu Q; Luo R A Poisson-Boltzmann Dynamics Method with Nonperiodic Boundary Condition. J. Chem. Phys 2003, 119, 11035–11047.

(67). Wang J; Cai Q; Li ZL; Zhao HK; Luo R Achieving Energy Conservation in Poisson-Boltzmann Molecular Dynamics: Accuracy and Precision with Finite-Difference Algorithms. Chem. Phys. Lett 2009, 468, 112–118. [PubMed: 20098487]

(68). Wang J; Luo R Assessment of Linear Finite-Difference Poisson-Boltzmann Solvers. J. Comput. Chem 2010, 31, 1689–1698. [PubMed: 20063271]

(69). Cai Q; Hsieh MJ; Wang J; Luo R Performance of Nonlinear Finite-Difference Poisson-Boltzmann Solvers. J. Chem. Theory Comput 2010, 6, 203–211. [PubMed: 24723843]

(70). Ye X; Wang J; Luo R A Revised Density Function for Molecular Surface Calculation in Continuum Solvent Models. J. Chem. Theory Comput 2010, 6, 1157–1169. [PubMed: 24723844]

(71). Cai Q; Ye X; Wang J; Luo R On-the-Fly Numerical Surface Integration for Finite-Difference Poisson-Boltzmann Methods. J. Chem. Theory Comput 2011, 7, 3608–3619. [PubMed: 24772042]

(72). Wang J; Cai Q; Xiang Y; Luo R Reducing Grid-Dependence in Finite-Difference Poisson-Boltzmann Calculations. J. Chem. Theory Comput 2012, 8, 2741–2751. [PubMed: 23185142]

(73). Wang C; Wang J; Cai Q; Li Z; Zhao HK; Luo R Exploring Accurate Poisson-Boltzmann Methods for Biomolecular Simulations. Comput. Theor. Chem 2013, 1024, 34–44. [PubMed: 24443709]

(74). Xiao L; Cai Q; Ye X; Wang J; Luo R Electrostatic Forces in the Poisson-Boltzmann Systems. J. Chem. Phys 2013, 139, 094106. [PubMed: 24028101]

(75). Wang CH; Xiao L; Luo R Numerical Interpretation of Molecular Surface Field in Dielectric Modeling of Solvation. J. Comput. Chem 2017, 38, 1057–1070. [PubMed: 28318096]

(76). Qi R; Botello-Smith WM; Luo R Acceleration of Linear Finite-Difference Poisson-Boltzmann Methods on Graphics Processing Units. J. Chem. Theory Comput 2017, 13, 3378–3387. [PubMed: 28553983]

(77). Wei H; Luo R; Qi R An Efficient Second-Order Poisson-Boltzmann Method. J. Comput. Chem 2019, 40, 1257–1269. [PubMed: 30776135]

(78). Qi R; Luo R Robustness and Efficiency of Poisson-Boltzmann Modeling on Graphics Processing Units. J. Chem. inf. Model 2019, 59, 409–420. [PubMed: 30550277]

(79). Fritsch FN; Carlson RE Monotone Piecewise Cubic Interpolation. SIAM Journal on Numerical Analysis 1980, 17, 238–246.

(80). de Boor C A Practical Guide to Splines; Springer-Verlag: New York, 1978.

(81). Moler CB Numerical Computing with Matlab; Society for Industrial and Applied Mathematics: Philadelphia, PA, 2004.

(82). Oliphant TE Python for Scientific Computing. Comput. Sci. Eng 2007, 9, 10–20.

(83). Meurer A; Smith CP; Paprocki M; Čertík O; Kirpichev SB; Rocklin M; Kumar A; Ivanov S; Moore JK; Singh S; Rathnayake T; Vig S; Granger BE; Muller RP; Bonazzi F; Gupta H; Vats S; Johansson F; Pedregosa F; Curry MJ; Terrel AR; Roučka S; Saboo A; Fernando I; Kulal S; Cimrman R; Scopatz A SymPy: Symbolic Computing in Python. Peer J. Computer Science 2017, 3, e103.

(84). Ulmschneider MB; Sansom MS Amino Acid Distributions in Integral Membrane Protein Structures. Biochim. Biophys. Acta, Biomembr 2001, 1512, 1 – 14.

(85). Kollman PA; Massova I; Reyes C; Kuhn B; Huo S; Chong L; Lee M; Lee T; Duan Y; Wang W; Donini O; Cieplak P; Srinivasan J; Case DA; Cheatham TE 3rd. Calculating Structures and Free Energies of Complex Molecules: Combining Molecular Mechanics and Continuum Models. Acc. Chem. Res 2000, 33, 889–897. [PubMed: 11123888]

(86). Gohlke H; Case DA Converging Free Energy Estimates: MM-PB(GB)SA Studies on the Protein-Protein Complex Ras-Raf. J. Comput. Chem 2004, 25, 238–250. [PubMed: 14648622]

(87). Srinivasan J; Cheatham TE; Cieplak P; Kollman PA; Case DA Continuum Solvent Studies of the Stability of DNA, RNA, and Phosphoramidate - DNA Helices. J. Am. Chem. Soc 1998, 120, 9401–9409.

(88). Miller BR; McGee TD; Swails JM; Homeyer N; Gohlke H; Roitberg AE MMPBSA.py: An Efficient Program for End-State Free Energy Calculations. J. Chem. Theory Comput 2012, 8, 3314–3321. [PubMed: 26605738]

(89). Wang C; Nguyen PH; Pham K; Huynh D; Le TB; Wang H; Ren P; Luo R Calculating Protein-Ligand Binding Affinities with MMPBSA: Method and Error Analysis. J. Comput. Chem 2016, 37, 2436–2446. [PubMed: 27510546]

(90). Wang C; Greene D; Xiao L; Qi R; Luo R Recent Developments and Applications of the MMPBSA Method. Front. Mol. Biosci 2018, 4, 87. [PubMed: 29367919]

(91). Pettersen EF; Goddard TD; Huang CC; Couch GS; Greenblatt DM; Meng EC; Ferrin TE UCSF Chimera–A Visualization System for Exploratory Research and Analysis. J. Comput. Chem 2004, 25, 1605–1612. [PubMed: 15264254]

(92). Xiao L; Wang C; Ye X; Luo R Charge Central Interpretation of the Full Nonlinear PB Equation: Implications for Accurate and Scalable Modeling of Solvation Interactions. J. Phys. Chem. B 2016, 120, 8707–8721. [PubMed: 27146097]

(93). Yang TY; Wu JC; Yan CL; Wang YF; Luo R; Gonzales MB; Dalby KN; Ren PY Virtual Screening Using Molecular Simulations. Proteins: Struct., Funct., Genet 2011, 79, 1940–1951. [PubMed: 21491494]

(94). Hou T; Wang J; Li Y; Wang W Assessing the Performance of the MM/PBSA and MM/GBSA methods. 1. The Accuracy of Binding Free Energy Calculations Based on Molecular Dynamics Simulations. J. Chem. Inf. Model 2011, 51, 69–82. [PubMed: 21117705]

(95). Marrink SJ; Sok RM; Berendsen HJC Free Volume Properties of a Simulated Lipid Membrane. J. Chem. Phys 1996, 104, 9090–9099.

(96). Sandoval-Perez A; Pluhackova K; Bockmann RA Critical Comparison of Biomembrane Force Fields: Protein-Lipid Interactions at the Membrane Interface. J. Chem. Theory Comput 2017, 13, 2310–2321. [PubMed: 28388089]

(97). Rocklin GJ; Mobley DL; Dill KA; Hunenberger PH Calculating the Binding Free Energies of Charged Species Based on Explicit-Solvent Simulations Employing Lattice-Sum Methods: An Accurate Correction Scheme for Electrostatic Finite-Size Effects. J. Chem. Phys 2013, 139, 184103. [PubMed: 24320250]

(98). Lin YL; Aleksandrov A; Simonson T; Roux B An Overview of Electrostatic Free Energy Computations for Solutions and Proteins. J. Chem. Theory Comput 2014, 10, 2690–2709. [PubMed: 26586504]

(99). Chen W; Deng Y; Russell E; Wu Y; Abel R; Wang L Accurate Calculation of Relative Binding Free Energies between Ligands with Different Net Charges. J. Chem. Theory Comput 2018, 14, 6346–6358. [PubMed: 30375870]

(100). Bennett WF; Tieleman DP The Importance of Membrane Defects-Lessons From Simulations. Acc. Chem. Res 2014, 47, 2244–2251. [PubMed: 24892900]

(101). Marrink SJ; de Vries AH; Tieleman DP Lipids on the Move: Simulations of Membrane Pores, Domains, Stalks and Curves. Biochim. Biophys. Acta, Biomembr 2009, 1788, 149–168.

(102). Gurtovenko AA; Anwar J; Vattulainen I Defect-Mediated Trafficking Across Cell Membranes: Insights From In Silico Modeling. Chem. Rev 2010, 110, 6077–6103. [PubMed: 20690701]

(103). Lazaridis T; Leveritt JM 3rd; PeBenito L Implicit Membrane Treatment of Buried Charged Groups: Application to Peptide Translocation Across Lipid Bilayers. Biochim. Biophys. Acta, Biomembr 2014, 1838, 2149–2159.

(104). Miloshevsky GV; Hassanein A; Partenskii MB; Jordan PC Electroelastic Coupling Between Membrane Surface Fluctuations and Membrane-Embedded Charges: Continuum Multidielectric Treatment. J. Chem. Phys 2010, 132, 234707. [PubMed: 20572734]

(105). Panahi A; Feig M Dynamic Heterogeneous Dielectric Generalized Born (DHDGB): An Implicit Membrane Model with a Dynamically Varying Bilayer Thickness. J. Chem. Theory Comput 2013, 9, 1709–1719. [PubMed: 23585740]

(106). Ravindranathan K; Tirado-Rives J; Jorgensen WL; Guimarães C R Improving MM-GB/SA Scoring Through the Application of the Variable Dielectric Model. J. Chem. Theory Comput 2011, 7, 3859–3865. [PubMed: 22606071]

(107). Lee MS; Olson MA Calculation of Absolute Protein-Ligand Binding Affinity Using Path and Endpoint Approaches. Biophys. J 2006, 90, 864–877. [PubMed: 16284269]

(108). Shirts MR; Mobley D; Brown SP Free-Energy Calculations in Structure-Based Drug Design. Drug Design: Structure and Ligand-based Approaches 2010, 61–86.

(109). Koes DR; Baumgartner MP; Camacho CJ Lessons Learned in Empirical Scoring with Smina from the CSAR 2011 Benchmarking Exercise. J. Chem. Inf. Model 2013, 53, 1893–1904. [PubMed: 23379370]

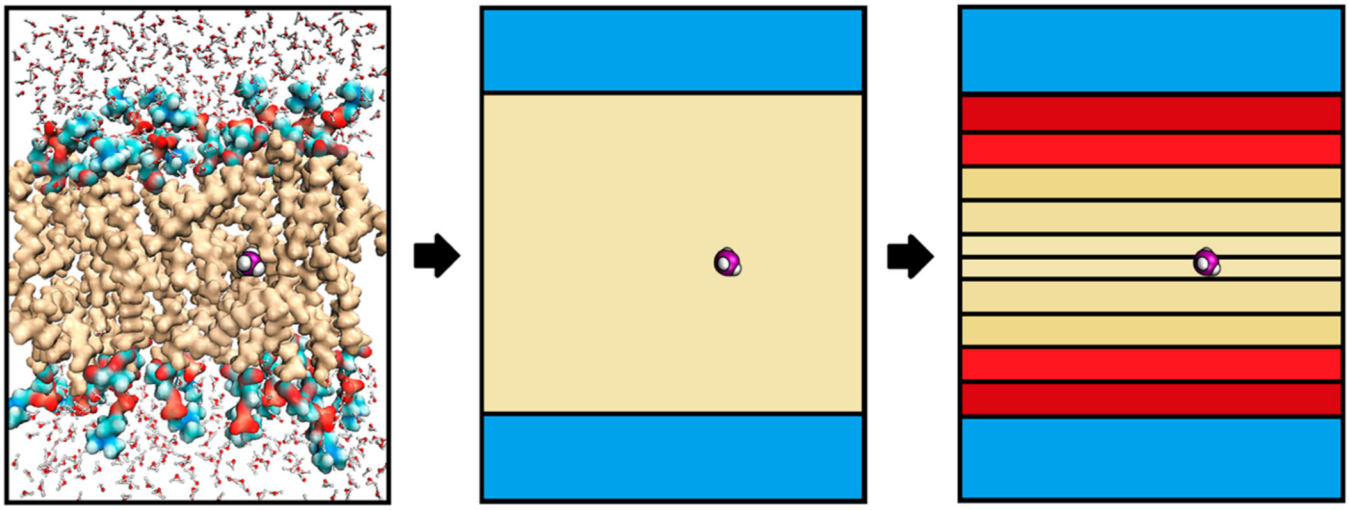

Figure 1.

Evolution of a heterogeneous dielectric implicit membrane model. An explicit solvent model (left) is first approximated by using an implicit solvent model where the solvent is treated as a dielectric continuum surrounding a molecule of interest, such as methane (purple and white). As a first approximation, the implicit solvent model (middle) may consist of an aqueous phase (blue) with a high dielectric constant and a single, uniform membrane slab region (tan) with a single, low dielectric constant. To better approximate the heterogeneous nature of the explicit phospholipid membrane, the implicit solvent model can be improved by dividing the membrane slab region into several small layers (right) with each layer containing a different value of the dielectric constant that has been optimized for that layer.

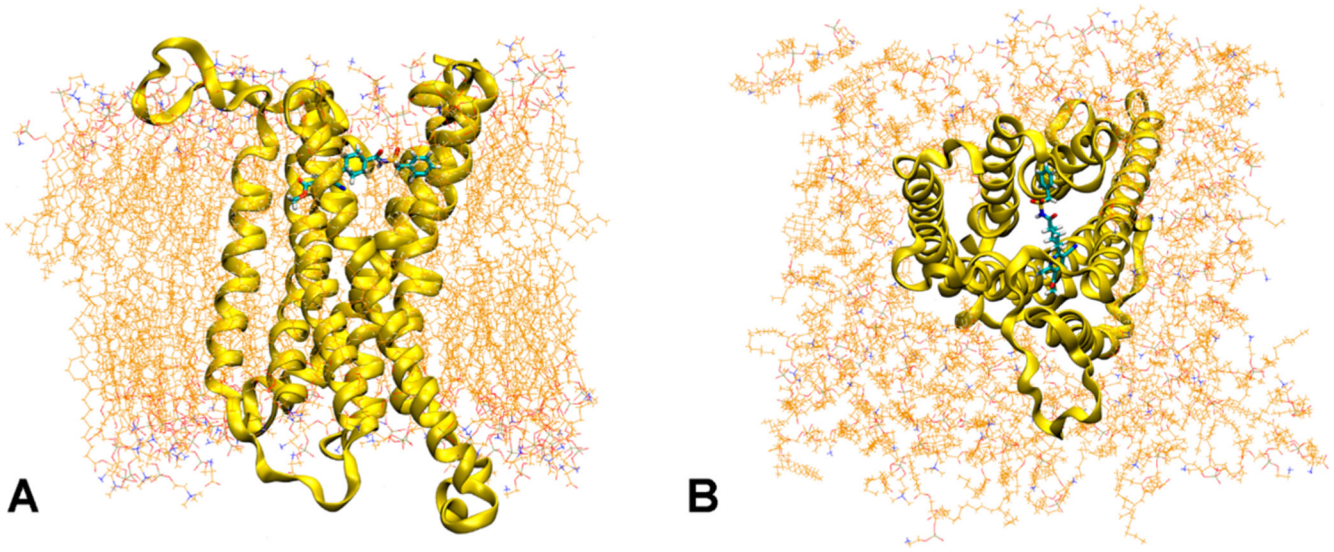

Figure 2.

Model of the antagonist-bound $P2Y_{12}R$ system used in our MD simulations. (A) Side view and (B) top down view of a snapshot taken from the production portion of the explicit MD trajectory for the $P2Y_{12}R$ receptor (yellow) bound to the AZD-1283 ligand (cyan). Nitrogen headgroup atoms that were used to calculate the average membrane thickness are shown in blue. Water has been omitted from this image for clarity.

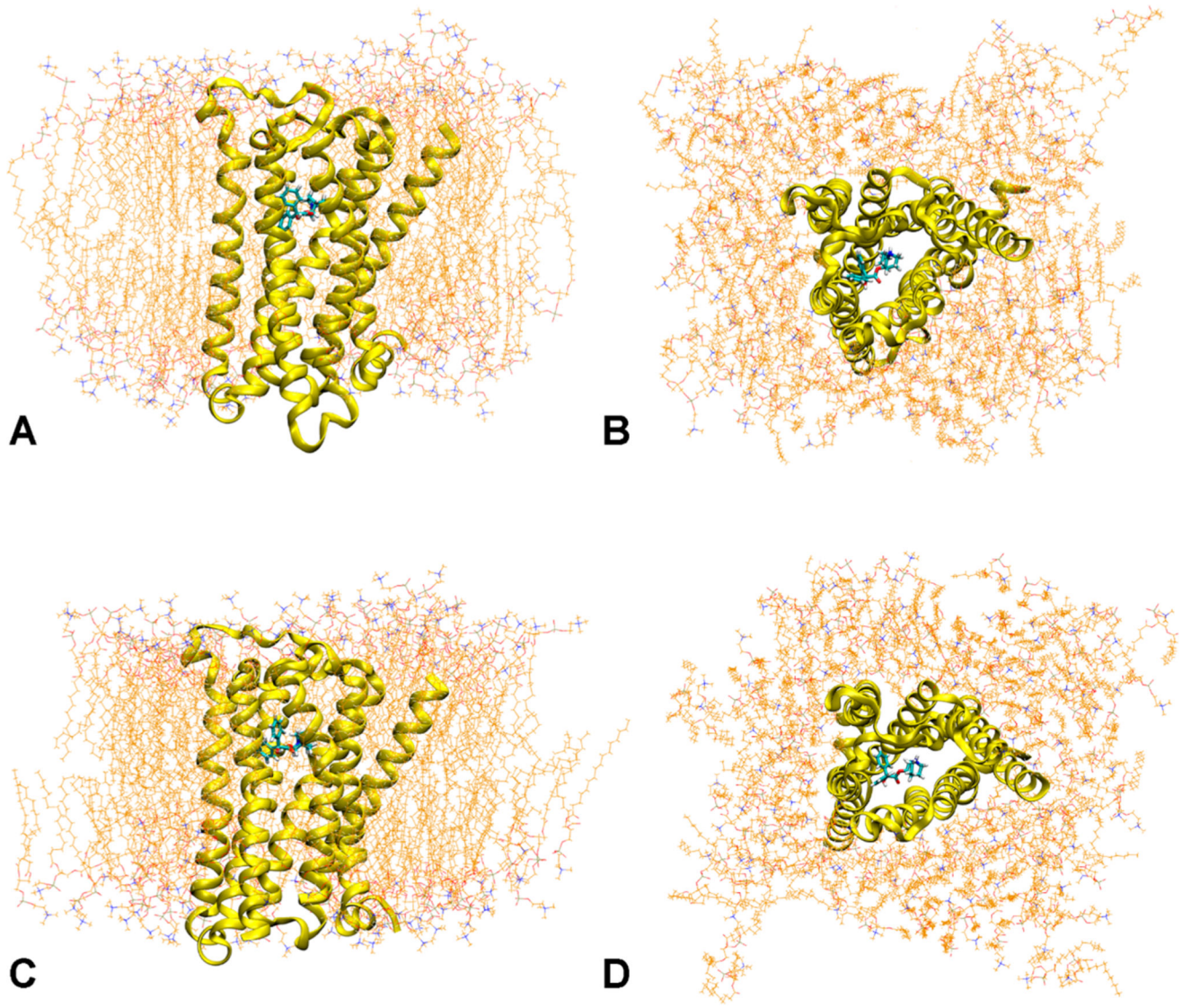

Figure 3.

Model of the antagonist-bound M2R and M3R systems used in our MD simulations. (A) Side view and (B) top down view of a snapshot taken from the production portion of the explicit MD trajectory for the M2R receptor (yellow) bound to the QNB ligand (cyan). (C) Side view and (D) top down view of a snapshot taken from the production portion of the explicit MD trajectory for the M3R receptor (yellow) bound to the QNB ligand (cyan). Nitrogen headgroup atoms that were used to calculate the average membrane thickness are shown in blue. Water has been omitted from this image for clarity.

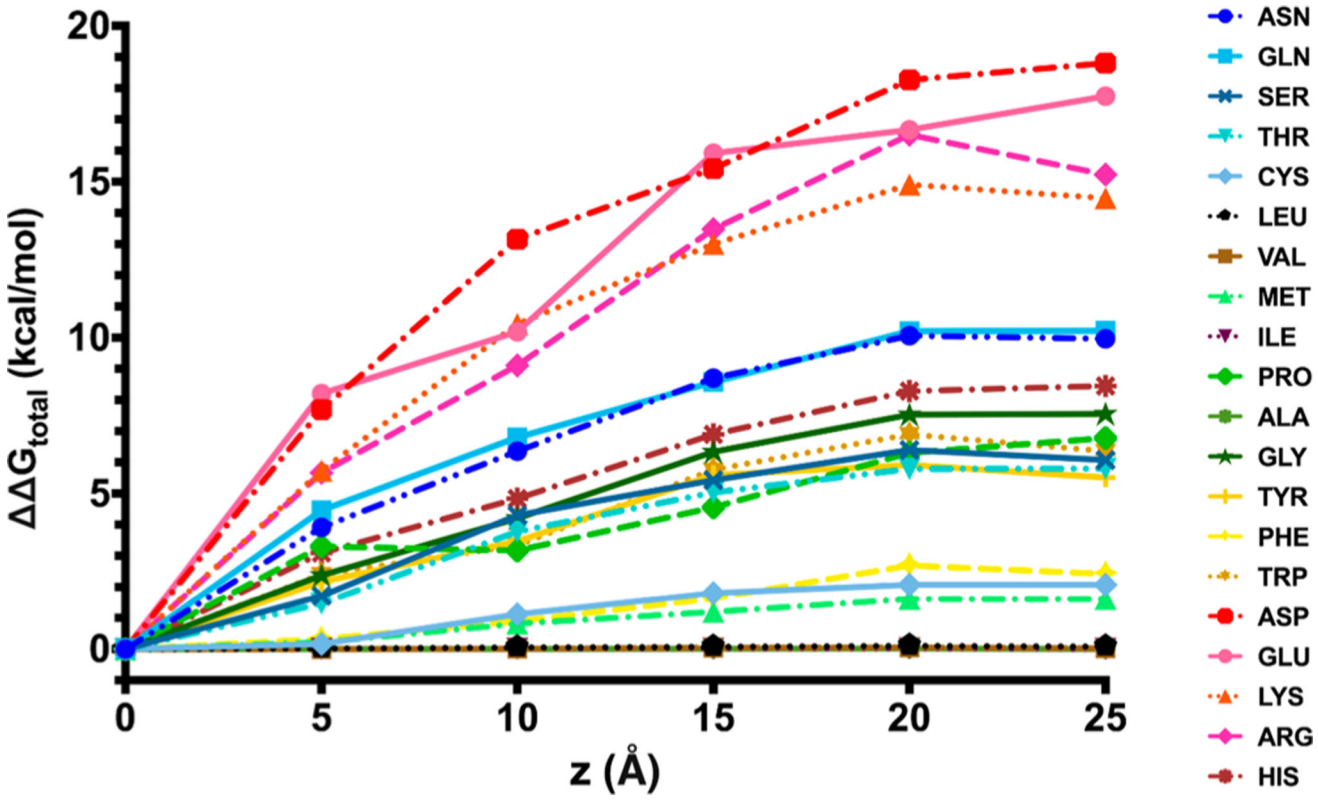

Figure 4.

Difference in ΔG_{total} values for decharging an amino acid side chain at height z. $\Delta\Delta G_{\text{total}}$ represents the net difference in the decharging free energy between placing an amino acid side chain at height z compared to placing it at the center of the membrane, at a height of z = 0 Å. The trend for each amino acid side chain is indicated using the standard three letter amino acid code. The trends for glycine and proline represent both the side chain and the amino acid backbone as the backbone was not removed in these two cases while the backbone was removed for all other amino acids.

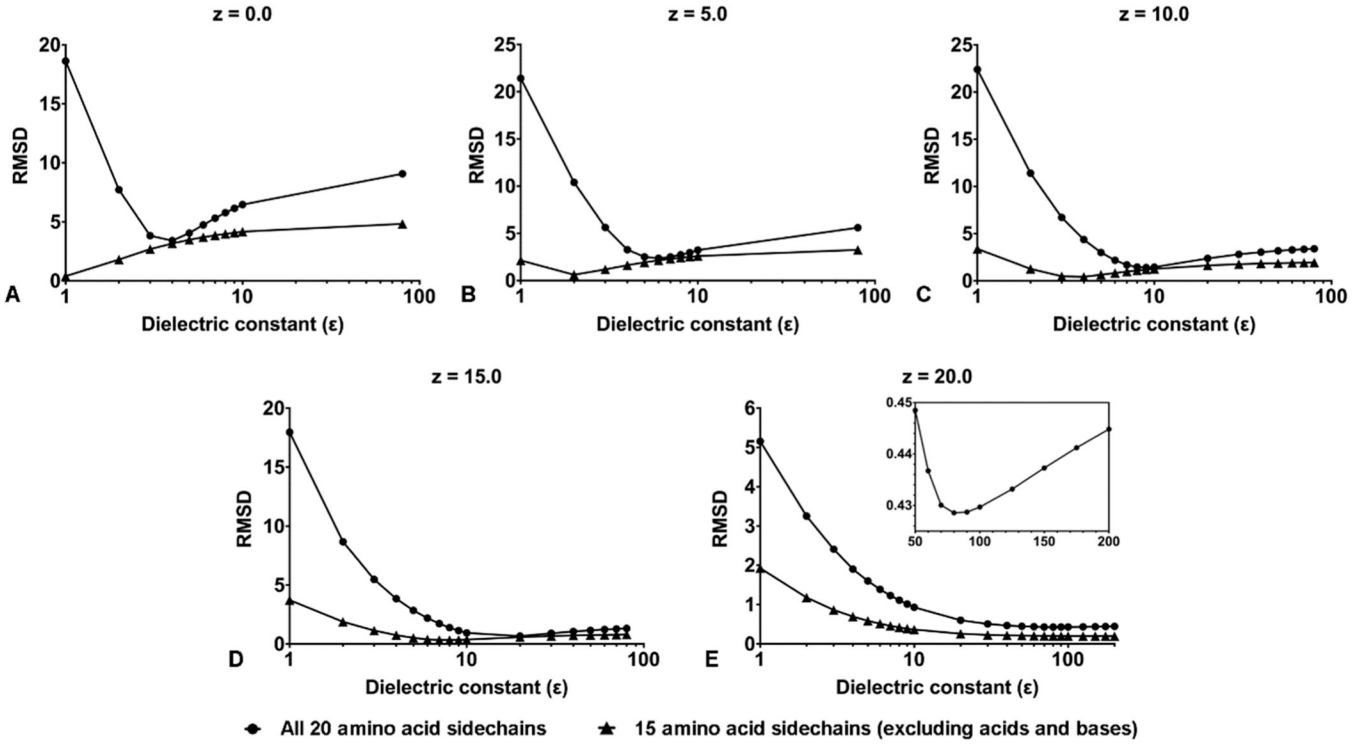

Figure 5.

RMSD between ΔG_{total} values calculated using PBSA-BAR and explicit BAR for various dielectric constants at different *z*-values. RMSD values were calculated using eq 7 over a set of amino acids using the following two schemes: (1) all 20 amino acid side chains (circles) and (2) 15 amino acid side chains, where all acidic and basic amino acids were excluded from the calculation (triangles). All RMSD values were reported in units of kcal/mol. All *z*-values (plots A–E) were given in units of Å. The *x*-axis was plotted logarithmically in order to fit a wide range of dielectric constant values on each plot.

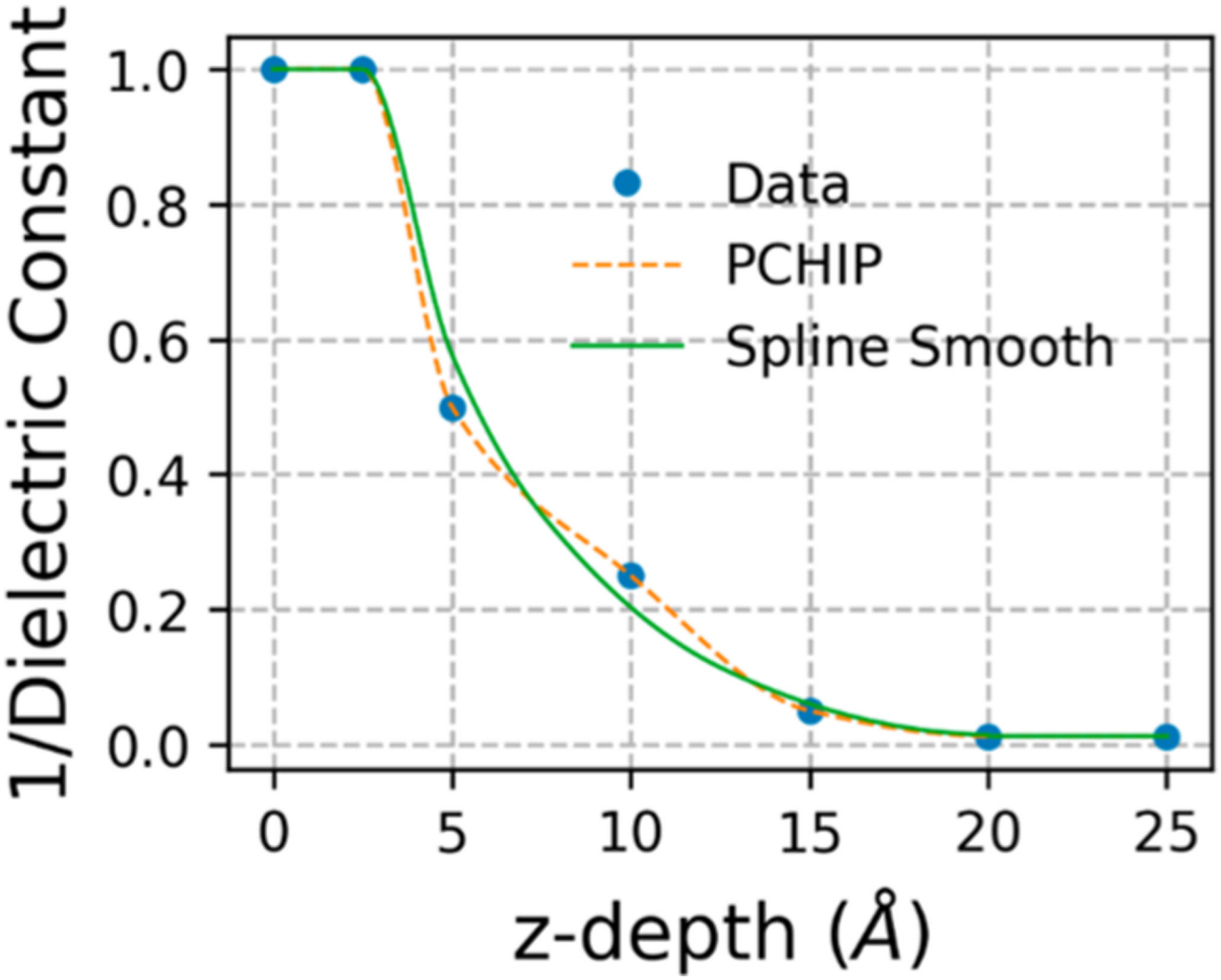

Figure 6.

PCHIP and spline fittings of a *z*-depth dependent membrane dielectric profile. Fittings for the dielectric constant are given in terms of the inverse dielectric constant ($1/\varepsilon$) while *z*-values are given with $z = 0$ Å corresponding to the center of the membrane and with $z = 25$ Å corresponding to the bulk aqueous solvent. The PCHIP fitting closely follows the trend established in the data, whereas the spline fitting has been smoothed.

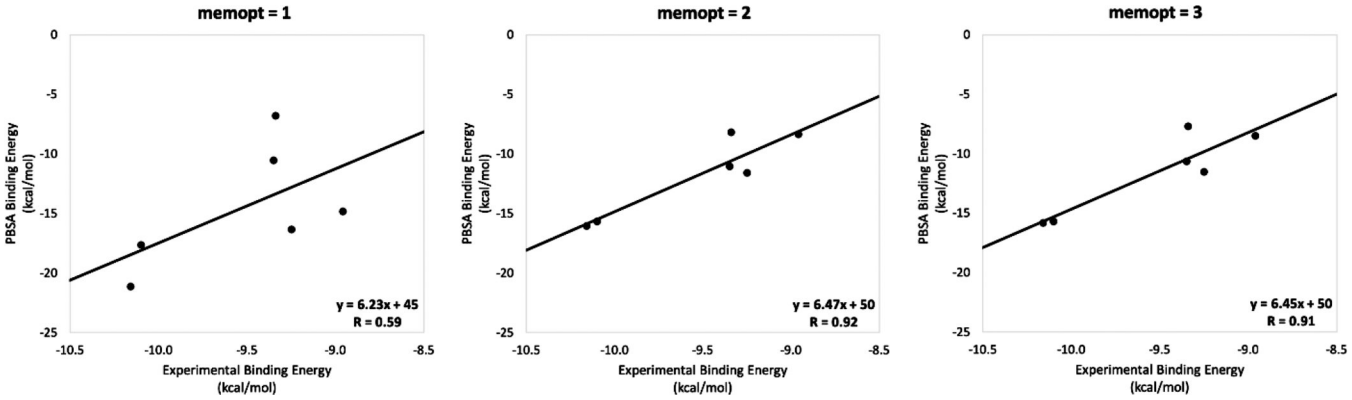

Figure 7.

Binding free energy correlation plots for the $P2Y_{12}R$ test system. PBSA binding free energy correlation plots are provided for the antagonist-bound $P2Y_{12}R$ system using the uniform, single dielectric membrane model (memopt = 1), the heterogeneous dielectric membrane model with the PCHIP fitting (memopt = 2), and the heterogeneous dielectric membrane model with the spline fitting (memopt = 3). For the uniform, single dielectric membrane model, the membrane dielectric constant was set to 4 while in all three models the protein dielectric constant was set to 2. The experimental binding free energies were obtained from the literature.[53]

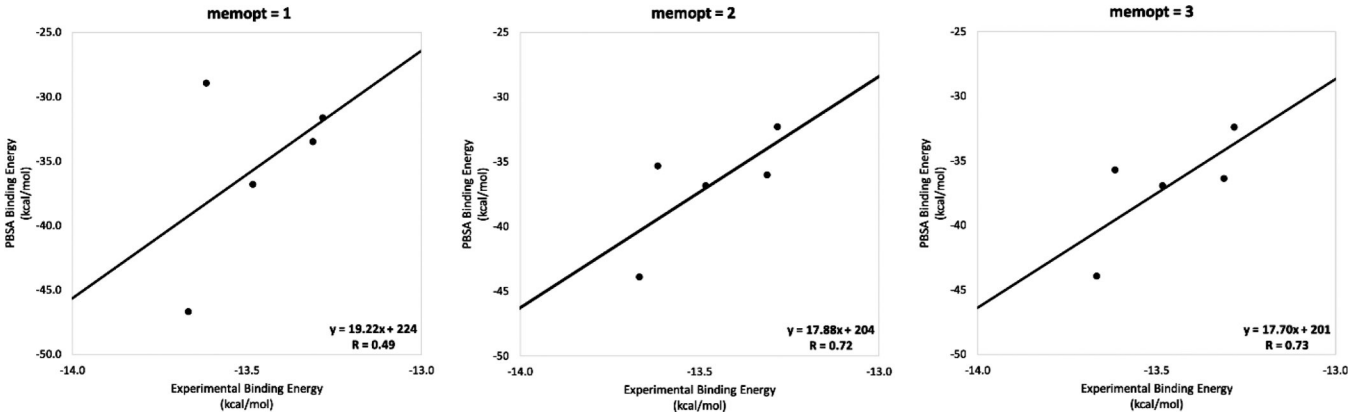

Figure 8.

Binding free energy correlation plots for the M2R/M3R test system. PBSA binding free energy correlation plots are provided for the antagonist-bound M2R/M3R test system using the uniform, single dielectric membrane model (memopt = 1), the heterogeneous dielectric membrane model with the PCHIP fitting (memopt = 2), and the heterogeneous dielectric membrane model with the spline fitting (memopt = 3). For the uniform, single dielectric membrane model, the membrane dielectric constant was set to 4 while in all three models the protein dielectric constant was set to 2. Note that the trend shown only contains five out of the six data points for the M2R/M3R test system as the M2R structure bound to C6B was a far outlier to the rest of the trend. The experimental binding free energies were obtained from the literature.[54]

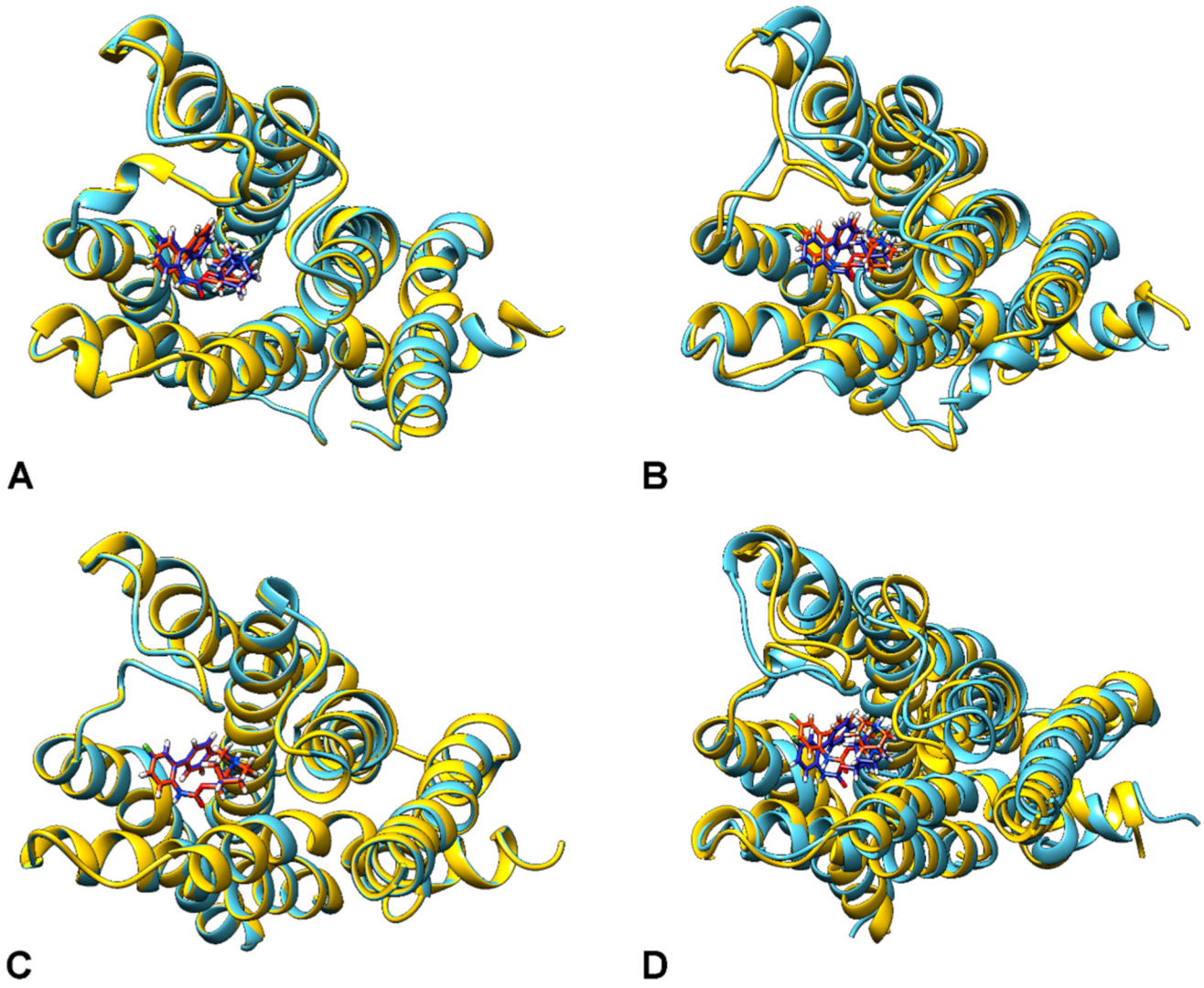

Figure 9.

Snapshots of compound 6B bound to the M2R and M3R receptors from our MD simulations. Aligned, superimposed snapshots of compound 6B bound to the M2R and M3R receptors were taken just before the heating step (image A for M2R and image C for M3R) and the very last frame of the production run (image B for M2R and image D for M3R) from the explicit MD trajectory. When the initial binding pose in the starting structure was based on the pose of QNB from the 3UON crystal structure, the receptors were shown in yellow and compound 6B was shown in orange. When the initial binding pose of compound 6B was determined by minimizing compound 6B in a vacuum environment before redocking it to the protein surface, the receptor was shown in cyan while compound 6B was given in dark blue. The structures were aligned with each other for this comparison using UCSF Chimera.[91]

Table 1.

Optimum Values of the Dielectric Constant within the Implicit Membrane[a]

z (Å)	method 1	method 2	method 3
0	4	1	1
5	6	2	2
10	9	4	4
IS	20	8	20
20	80	>200	80

[a]Initially, two dielectric profiles were constructed based on the method for calculating the RMSD using eq 7: method 1, where all 20 amino acid side chains were used to find the optimum dielectric constant at each *z*-value, and method 2, where 15 amino acid side chains were used to find the optimum dielectric constant, with all acidic and basic amino acids excluded from this calculation at all depths. For the final profile (method 3), we used the optimized dielectric values from method 1 for $z = 15$ and 20 Å, and from method 2 for $z = 0$, 5, and 10 Å.

Table 2.

RMSD Results for PBSA-BAR Calculations Using the Heterogeneous Dielectric Membrane Model[a]

	RMSD all 20 amino acids		RMSD 15 AAs (no acidic or basic AAs)	
z **(Å)**	**memopt = 2**	**memopt = 3**	**memopt = 2**	**memopt = 3**
0	11.256	11.978	0.579	0.431
5	6.196	6.112	0.796	0.785
10	1.204	1.237	0.732	0.778
15	0.667	0.580	0.631	0.590
20	0.493	0.5SS	0.2S1	0.263
25	0.049	0.056	0.015	0.013

[a]The results of PBSA-BAR calculations using the heterogeneous dielectric implicit membrane model with the PCHIP fitting (memopt = 2) and the spline fitting (memopt = 3). RMSD values for this data set were calculated using eq 7. The first and second columns give the RMSD values for calculations that included all 20 amino acid side chains while the third and fourth columns omit all of the acidic and basic amino acid side chains in the RMSD calculations. All RMSD values are reported in units of kcal/mol.

Table 3.

Results of MMPBSA Calculations for Antagonist Ligands Bound to $P2Y_{12}R$[a]

	Δ*G*(MMPBSA)			
structure	**memopt = 1**	**memopt = 2**	**memopt = 3**	**Δ*G*(exp.)**
$P2Y_{12}R$ WT (AZD)	−21.1	−16.0	−15.8	−10.16
$P2Y_{12}R$ D294N (AZD)	−17.6	−15.6	−15.7	−10.10
$P2Y_{12}R$ WT (PSB)	−10.S	−11.0	−10.6	−9.35
$P2Y_{12}R$ D294N (PSB)	−6.8	−8.2	−7.6	−9.34
$P2Y_{12}R$ WT (TIQ)	−14.8	−8.3	−8.4	−8.96
$P2Y_{12}R$ D294N (TIQ)	−16.3	−11.6	−11.5	−9.25

[a]MMPBSA calculations were carried out using SANDER in MMPBSA.py for the $P2Y_{12}R$ test system using the uniform, single dielectric membrane model (memopt = 1), the heterogeneous dielectric membrane model with the PCHIP fitting (memopt = 2), and the heterogeneous dielectric membrane model with the spline fitting (memopt = 3). For the uniform, single dielectric membrane model, the membrane dielectric constant was set to 4 while in all three models the protein dielectric constant was set to 2. The experimental binding free energies were obtained from the literature.[53] WT refers to the wildtype structure of $P2Y_{12}R$ while D294N refers to the mutant structure of $P2Y_{12}R$. The antagonist ligand bound to $P2Y_{12}R$ is listed in parentheses. All binding free energies are reported in units of kcal/mol.

Table 4.

Results of MMPBSA Calculations for Antagonist Ligands Bound to M2R and M3R[a]

	Δ*G*(MMPBSA)			
structure	**memopt = 1**	**memopt = 2**	**memopt = 3**	**Δ*G*(exp.)**
M3R (QNB)	−28.9	−35.3	−35.7	−13.6
M3R (TIO)	−31.6	−32.3	−32.4	−13.3
M3R (C6B)	−33.4	−36.0	−36.3	−13.3
M2R(QNB)	−46.7	−43.9	−43.9	−13.7
M2R (TIO)	−36.8	−36.8	−36.9	−13.5
M2R (C6B)[b]	−38.4	−36.2	−36.5	−10.5

[a]MMPBSA calculations were carried out using SANDER in MMPBSA.py for the M2R and M3R test system using the uniform, single dielectric membrane model (memopt = 1), the heterogeneous dielectric membrane model with the PCHIP fitting (memopt = 2), and the heterogeneous dielectric membrane model with the spline fitting (memopt = 3). For the uniform, single dielectric membrane model, the membrane dielectric constant was set to 4 while in all three models the protein dielectric constant was set to 2. The experimental binding free energies were obtained from the literature.[54] The antagonist ligand bound to M2R or M3R is listed in parentheses. All binding free energies are reported in units of kcal/mol.

[b]This was excluded from Figure 8.